HIGH-RESOLUTION DYNAMICAL DOWNSCALING OF PAST AND FUTURE CLIMATE OF THE WESTERN UNITED STATES: VALIDATION OF PERFORMANCE AND ANALYSIS OF CHANGING SNOWPACK

by

Jason Scalzitti

A thesis submitted to the faculty of
The University of Utah
in partial fulfillment of the requirements for the degree of

Master of Science

Department of Atmospheric Sciences

The University of Utah

May 2016

The University of Utah Graduate School

STATEMENT OF THESIS APPROVAL

The thesis of **Jason Scalzitti**

has been approved by the following supervisory committee members:

Courtenay Strong	, Chair	**03/04/16** Date Approved
William James Steenburgh	, Member	**03/04/16** Date Approved
Adam Krzysztof Kochanski	, Member	**03/04/16** Date Approved

and by **Kevin Perry** , Chair/Dean of

the Department/College/School of **Atmospheric Sciences**

and by David B. Kieda, Dean of The Graduate School.

ABSTRACT

A 26-year high-resolution dynamical downscaling over the Wasatch Mountains of Utah, USA was performed using the Weather Research and Forecasting (WRF) model with initial and boundary conditions derived from Climate Forecast System Reanalysis (CFSR). Precipitation validation was conducted on the inner (4-km resolution) domain with Snowpack Telemetry (SNOTEL) and Parameter-elevation Regressions on Independent Slopes Model (PRISM) data sets. Analysis of seasonal performance reveals the model's overall good skill at reproducing the spatial distribution of precipitation. Annual precipitation validates within ∼20% of SNOTEL. The largest monthly biases occurred in December-January (∼+30%). Composite analysis of cold season days with large positive or negative precipitation biases reveals two distinct synoptic regimes with significantly different moisture, temperature, and circulation patterns that respectively enhanced geopotential height and moisture biases consistent with the sign of their mean precipitation biases. The number of cold season days with large (>5 mm) positive precipitation bias was negatively correlated with El Niño ($r = -0.55$), indicating storm track-related effects on the sign of the bias consistent with the distinct synoptic regimes revealed by the above-noted composite analyses.

This historical simulation was compared with a pseudo-global warming simulation of climate change to evaluate the roles of temperature and precipitation in spring snowpack (S) variability across the western United States. In both historical and future climate, the negative correlation between S and temperature weakens linearly with elevation whereas the correlation between S and precipitation increases logarithmically with elevation. The curvilinear relationship in the latter case was not visible in prior studies because of the observation networks' limited range. In the historical simulation, there is a range of threshold elevations (1574-2119 m) above which precipitation is the main driver of snowpack variability and below which temperature is the main driver. Under a moderate end-of-century climate change scenario, these thresholds increase by 239-447 m across six mountainous regions (317 m on average). These rising thresholds indicate increasing spatial and elevational vulnerability of western U.S. spring snowpack along with associated impacts to hydrologic and ecologic systems.

TABLE OF CONTENTS

LIST OF FIGURES

LIST OF TABLES

ACKNOWLEDGEMENTS

The first author gratefully acknowledges the support of the U.S. Air Force Institute of Technology program. The views expressed in this thesis are those of the author and do not reflect the official policy or position of the U.S. Air Force, Department of Defense, or the U.S. government. Computing resources (ark:/85065/d7wd3xhc) were provided by the Climate Simulation Laboratory at NCAR's Computational and Information Systems Laboratory, sponsored by the National Science Foundation and other agencies. Provision of additional computer infrastructure by the Center for High Performance Computing at the University of Utah is also gratefully acknowledged. This material is partially based upon work supported by the National Science Foundation under grants EPS-1135482, EPS-1135483, and EPS-1208732. Any opinions, findings, and conclusions or recommendations expressed in this material are those of the author and do not necessarily reflect the views of the National Science Foundation.

CHAPTER 1

INTRODUCTION

This introduction is composed of two sections, the first being a literature review and overview of the motivation for dynamically downscaling historical climate over the Wasatch Mountains. The second section outlines the motivation for modeling of future climate for comparison to the historical simulation leading to an assessment of climate change impact on snowpack variability in the western United States.

1.1 Motivation for Historical Climate Simulation

Wintertime precipitation and its resultant seasonal snowpack development remain critically important to the economies and livelihood of the communities of the Intermountain West. For much of the region, springtime runoff from snowmelt controls the hydrologic balance, and accurate knowledge of both the historical trends and future changes in the spatial and temporal pattern of mountain precipitation is vital to water resource management. One region particularly vulnerable to changes in snowpack-supplied water resources is the eastern edge of the Great Basin, USA, where approximately two million people reside along the front of the Wasatch Mountains.

Salt Lake City and its growing population (+0.86% yr^{-1}) reside downstream from watersheds where snowmelt provides 72% of total annual runoff. Considering that 50% of Salt Lake City's water supply emerges from just four streams feeding from the adjacent Wasatch Mountains, growing concern over changes in the future amount and timing of runoff reinforces the need to accurately simulate seasonal precipitation in these mountains (Bardsley et al., 2013).

Much of the urgency surrounding this issue stems from concern that climate change will impact the intensity, spatial distribution, and timing of wintertime precipitation and its associated snowpack development. Studies of historical trends generally point to an increasing proportion of wintertime precipitation falling as rain rather than snow in the western US (Knowles et al., 2006; Gillies et al., 2012). A good deal of certainty supports the expected increase in wintertime precipitation at high latitude areas of North America across a range of greenhouse gas emission scenarios (Christensen et al., 2013), but the certainty in both magnitude and sign decreases southward to a zonally-oriented zero-change transition zone across or close to Utah. The Fifth Intergovernmental Panel on Climate Change (IPCC) Assessment Report (AR5) also places this transition between the wetter US northern tier and drier US Southwest tier very close to Utah (see Fig. TS.13 in (Stocker et al., 2013)). Bardsley et al. (2013) highlight this concern for the Wasatch region, noting the range of magnitudes and competing signs in the General Circulation Model (GCM) projections of mid-century precipitation changes. Much of this uncertainty stems from the GCM's coarse scales, which do not adequately represent complex

topography like that found at the headwaters of the rivers feeding Salt Lake City's reservoirs. It is generally believed that higher-resolution handling of topography may resolve associated meso- and micro-scale processes, thereby delivering greater confidence in future hydroclimate trends.

Statistical downscaling of GCMs offers one method for delivering finer-scale information on a point or regional domain by transforming the coarse GCM fields (∼50 to 100's of km resolution) to finer-scale grids. One such downscaling study over the mountains of the Western US by Pierce and Cayan (2012) applies a bias correction with constructed analog (BCCA) technique offered by Maurer et al. (2010) and Hidalgo et al. (2008), and delivers 1/8° X 1/8° output for hydroclimate analysis. Their results show that across a range of CO_2 emission scenarios, cold season precipitation over the Wasatch will increase in the range of 5-15% by the end of the 21st century. For the lowest emission scenario (RCP 4.5), however, only ∼45% of AR5 models feature a statistically significant increasing trend in Wasatch cold season precipitation by the end of century. This value increases to ∼80% of AR5 models for the highest emission scenario (RCP 8.5). Other studies highlight inconsistencies among statistically downscaled GCM output as to the magnitude and sign of future change in precipitation across the Intermountain West (Deser et al., 2012; Harding et al., 2012). Analysis of historical trends in downscaled AR5 models by Kumar et al. (2013) emphasizes their poor handling of long-term precipitation trends as well.

Alternatively, a regional climate model (RCM) may be used to dynamically downscale boundary conditions provided by reanalysis data in the past or GCM

output in the past or future. Yoon et al. (2012) showed that this strategy improves performance with respect to statistical GCM downscaling in cold season precipitation prediction in the USA, but improvements vary by geographic region. Dynamical downscaling with the Weather Research and Forecasting (WRF) model over the mountains of Colorado has recently been shown to capture fine-scale processes over complex topography, a capability which eludes statistical downscaling methodology (Gutmann et al., 2012). Several studies have recently evaluated the merits of dynamical downscaling techniques over the western half of North America, i.e., Caldwell et al. (2009) over California, Ikeda et al. (2010) and Rasmussen et al. (2011a) over Colorado, and Erler et al. (2014) over Western Canada. Ikeda et al. (2010), for example, applied a downscaling technique over a domain with 2-km grid spacing in the Colorado Headwaters where WRF validated within 10-15% for most wintertime months' accumulated precipitation, with monthly values within 20% for 71% of the time.

Chapter 2 describes an historical simulation which applies this dynamical downscaling methodology and assesses its performance in accurately modeling precipitation over the Wasatch Mountains. Additionally, its wintertime precipitation biases are analyzed and partly explained according to composite synoptic analysis. The results presented in Chapter 2 have been conditionally accepted in the *Journal of Geophysical Research-Atmospheres*.

1.2 Motivation for Future Climate Simulation

Seasonal snowfall in the mountainous regions of the western United States is a critical component of the annual water cycle as regional water supplies rely heavily on spring and summer melt from the accumulated snowpack. Many studies have identified widespread declines in snowpack in western North America (Hamlet et al., 2005; Mote et al., 2005; Mote, 2006), and these changes have been linked to warming trends (Pederson et al., 2011; Kapnick and Hall, 2012; Pederson et al., 2013) and increasing freezing-level elevations (Abatzoglou, 2011). Additionally, approximately half of recent changes in western U.S. snowpack have been attributed to anthropogenic effects (Pierce et al., 2008). Future projections of snow water equivalent (SWE) point to widespread losses across the western U.S. (Brown and Mote, 2009; Peacock, 2012; Pierce and Cayan, 2012), findings that complement modeling studies showing a widespread transition from a largely snow-dominant to a rain-dominant precipitation regime (Klos et al., 2014).

To investigate these phenomena, many studies have utilized temperature and precipitation as predictors of SWE, both in relatively simple snow models (Wolock and McCabe, 1999; McCabe and Wolock, 2010; Pederson et al., 2013) and regression analysis (Cayan, 1996; Mote, 2006; Morán-Tejeda et al., 2013; Sospedra-Alfonso et al., 2015). Analyzing three mountainous regions of Switzerland, Morán-Tejeda et al. (2013) found that the negative correlation between temperature and snowpack variability weakens linearly with elevation, whereas the positive correlation between precipitation and snowpack variability increases linearly with elevation. They charac-

terized the relative roles of temperature and precipitation by identifying an elevation threshold (1400 ± 200 m) above which precipitation is the main driver of snowpack variability and below which temperature is the main driver. Additionally, they identified a rising trend in this threshold over the period 1976-2011 for certain snowpack indices, but that trend was not significant for April snow depth. These varying trends were associated with generally rising but variable inter-annual temperature trends over that same period. Sospedra-Alfonso et al. (2015) extended this analysis to a region of the Rocky Mountains encompassing northern Idaho and northwestern Montana. Their analysis differed from Morán-Tejeda et al. (2013) in that they applied a lapse rate adjustment to their temperature data in order to analyze a larger, more thermally heterogeneous domain. Additionally, they identified a higher elevation threshold for temperature- and precipitation-driven snowpack variability (1578 ± 76 m for April mean SWE) over their study domain and emphasized the need to understand the effects of a changing climate on this threshold.

Chapter 3 features a study which adapts and applies these analyses to six subregions of the western U.S. and extends this framework to assess the changing relative roles of temperature and precipitation in driving spring snowpack variability under a moderate climate change perturbation at the end of the 21st century. The analysis and results presented in Chapter 3 have been submitted to *Geophysical Research Letters*. Chapter 4 includes the discussion and conclusions for Chapters 2 and 3.

CHAPTER 2

VALIDATION OF HISTORICAL SIMULATION

2.1 Introduction

The importance of Wasatch Mountain wintertime precipitation to the livelihood of those living along the Wasatch Front motivated centering a high-resolution dynamical downscaling simulation over Utah with an explicit model of the Great Salt Lake to accurately capture lake effects. This simulation of historical climate from 1985-2010 (26 years, 25 water years) was performed to test the downscaling methodology within a domain centered on the Wasatch Mountains. We evaluated the performance of this retrospective simulation, seeking to gain confidence in this technique for simulation of future climate. We define the configuration of our simulation as well as the data used to validate its performance in section 2.2. In section 2.3, we evaluate simulated precipitation using multiple validation data sets. These simulation precipitation biases are modest and associated with distinct synoptic regimes with associated moisture, temperature, wind speed, and geopotential height biases with respect to the forcing reanalysis. Summary and conclusions are presented in section 2.4.

2.2 Data and Methods

2.2.1 Model Configuration

The downscaling model is WRF version 3.3.1 (Skamarock et al., 2008) configured with the Noah land surface model (LSM) (Chen and Dudhia, 2001), Mellor-Yamada-Janjic (MYJ) planetary boundary layer scheme (Janjić, 2002), Thompson et al. (2008) cloud microphysics scheme, and the Community Atmosphere Model (CAM) longwave and shortwave schemes (Collins et al., 2006). The Betts-Miller-Janjić convective parameterization was activated on the coarser middle and outer domains (Janjic, 1994).

We customized this configuration, which follows that of Ikeda et al. (2010) and Rasmussen et al. (2011a), in several ways. First, the model's innermost domain was coupled with a slab lake model for the Great Salt Lake (GSL) developed by Strong et al. (2014) to better evaluate the regional impacts of this large, hypersaline lake on Wasatch precipitation. In a sensitivity analysis, the slab model developers coupled a 5-m effective mixing depth for the GSL with WRF and accounted for at least 97% of the GSL surface temperature variance as observed by the MODIS-Terra satellite platform over a two-yr period. Additionally, the GSL slab lake/WRF coupling reduced downstream springtime precipitation bias compared to a simulation with prescribed GSL surface climatology. With an approximate surface area of 4400 km^2, the GSL's surface temperature influences downstream snowpack development through lake effect snow (Steenburgh et al., 2000; Alcott et al., 2012; Yeager et al., 2012), and better representation of the GSL by this slab model therefore improves

WRF precipitation output skill.

The second adjustment to the configuration involved the tuning of soil moisture thresholds in the Noah LSM to better align with WRF's urban latent heat flux using Salt Lake Valley eddy covariance measurements (Ramamurthy and Pardyjak, 2011) as further described in Strong et al. (2014). Finally, following Steenburgh and Onton (2001), we decreased vapor pressure (q_s) over the GSL to account for its dual salinity characteristics, applying $0.70q_s$ over the more saline north portion of the lake and $0.94q_s$ over the south portion of the lake.

We configured WRF with three one-way nested domains with increasing resolution moving inward from 36-km to 12-km to 4-km grid spacings (Fig. 2.1a). The choice of 4-km grid spacing follows the findings of the previously-mentioned climate modeling study by Ikeda et al. (2010), which showed that sub-6 km resolution reasonably simulates snowfall over the complex terrain of the Colorado Headwaters mountains. Initial conditions at the surface, atmosphere, and lateral boundary were derived from 6-hrly Climate Forecast System Reanalysis (CFSR) (Saha et al., 2010) at 38 km resolution. For each of the 26 years, we re-initialized all atmospheric variables on 0000 UTC of 1 January and carried over the previous year's 2300 UTC 31 December values for snowpack, soil moisture, soil temperature, and skin temperature.

2.2.2 Verification Data

Our validation of model output focuses on the Wasatch Mountains and the western edge of the Uintah Mountains (red outline in Fig. 2.1) due to importance to

the region's water resources. Our primary observation tool for validating model data in this region was SNOTEL, a network of high-elevation automated sensors operated by the National Resources Conservation Service (NRCS) branch of the Department of Agriculture (USDA). A commonly-cited limitation to this data set's reliability is the wind-driven undercatch by the precipitation gauge. Serreze et al. (1999) offers a description of the SNOTEL network, highlighting the Alter wind shield and its ability to increase catch efficiency of the precipitation gauge. Yang et al. (1998) offers regression-based adjustments based on gauge-height wind speeds to persistent wind-driven undercatch (i.e., $\sim$11% undercatch for 2 m s^{-1} wind speeds). However, larger biases may occur, with snowfall more susceptible than rainfall (Groisman and Easterling, 1994). A field experiment conducted by Rasmussen et al. (2011b) found that Alter-shielded gauges underestimated snow accumulation by more than 30% in an intense snowstorm at a Colorado field site. Our comparison of modeled precipitation with SNOTEL data is therefore susceptible to this source of error, and some proportion of cold season biases may be attributable to SNOTEL undercatch. Other factors influencing SNOTEL's measurement biases include vegetation changes, land-use changes, and sensor upgrades. For example, Julander and Bricco (2006) attribute approximately 10% undercatch at the central Wasatch Brighton SNOTEL station to the installation of a wide, four-person chair lift on both sides of the site. Another relevant consideration is the 0.1 inch resolution of SNOTEL precipitation measurements. Since SNOTEL does not record sub-0.1 inch precipitation amounts, trace values (i.e., $0.01 < 0.1$) of precipitation in WRF's high-resolution hourly output

could accumulate over the course of a winter to non-negligible biases.

SNOTEL site suitability for validation was assessed based upon an objective geographic boundary and period of sensor activity. A sub-section of the innermost 4-km domain (red outline, Fig. 2.1b) constrains SNOTEL site selection for Wasatch precipitation verification to a geographic region of hydrologic importance to Salt Lake City. This SNOTEL subdomain spans the Wasatch Mountain north-south extent within the Great Basin drainage area. Its eastern boundary aligns with the eastern edge of the Great Basin which drains westward into these valleys, and its western boundary includes the important Oquirrh and Stansbury Mountains southwest of Salt Lake City. Of the 34 SNOTEL sites inside of this SNOTEL subdomain which began operating before 1991 (>80% of the simulated water years), 28 were active for the entire time period covered by the historical runs (1985-2010). Six additional sites (yellow circles in Fig. 2.1b) were added to the validation starting in the year each became active, with all 34 sites applied from 1990 onwards. Three of those six additional sites provide coverage for at least 80% of the simulated water years over the key central Wasatch streams responsible for over half of Salt Lake City's water supply. A bi-linear interpolation of WRF precipitation values at neighboring grid points to each SNOTEL site was used to compare with the SNOTEL observations. Comparison was made to the single nearest grid point value as well, and the results did not differ significantly (results not shown). Daily mean WRF and SNOTEL values for the SNOTEL subdomain are compared first according to the 24-hr SNOTEL day which begins at midnight Pacific Standard Time (08 UTC) before being summed to seasonal

and annual totals.

For overall spatial verification of the inner domain, we present Parameter-elevation Regressions on Independent Slopes Model (PRISM) data (Daly et al., 1994, 1997, 2002, 2008). This data set is available from the PRISM Climate Group, Oregon State University (http://prism.oregonstate.edu), and applies a simple factor-weighted climate-elevation regression on a digital elevation model. Each observation sensor whose data enters the model is weighted according to parameters such as elevation, location, topography, coastal proximity, and vertical atmospheric layer. The PRISM technique fundamentally assumes, though, that elevation is the most important influence on precipitation distribution (Daly et al., 2008). It should be noted that SNOTEL and PRISM are not independent data sets, as SNOTEL data is a component of PRISM, so the temporal (SNOTEL) and spatial (PRISM) validations are subject to the same potential SNOTEL measurement errors with potentially additional errors from PRISM's factor weighted regression. PRISM data were obtained monthly on a 4-km resolution grid, which we interpolated onto our model's innermost 4-km domain for point-to-point spatial comparison.

2.3 Results

2.3.1 Historical Validation

Validation of the overall spatial representation of WRF precipitation is presented in Fig. 2.2a-c as maps of climatology for water year accumulated precipitation from WRF, PRISM, and the difference between the two (water year is 1 October of year

prior through 30 September of water year). Broad spatial correlation can be seen with respect to the underlying topography. Overall modest differences between the WRF and PRISM sets indicates WRF's general skill at simulating water year precipitation with errors of $+/-200$ mm and isolated errors up to 400 mm in regions of the Wasatch Mountains. Fig. 2.2d-f focus this same comparison to only cold season (1 November–31 March) accumulated precipitation. A more pronounced positive bias pattern emerges in the cold season difference map compared to the water year differences, particularly the over-prediction by WRF across more of the Wasatch subdomain, with widespread biases up to $\sim$200 mm and isolated regions up to $\sim$400 mm. Note that the overall spatial distribution of cold season precipitation is still well-represented by WRF (Fig. 2.2d).

In Fig. 2.3, we present a comparison of WRF and SNOTEL average precipitation for each of 34 SNOTEL sites. For the cold season (yellow filled circles in Fig. 2.3), the position of the majority of points above the one-to-one line is consistent with the previously noted tendency for positive precipitation bias, but WRF correlates well with SNOTEL ($r = 0.85$, $p < 0.01$) with a root-mean-squared error (RMSE) of 73.1 mm. Gutmann et al. (2012), who applied a very similar downscaling configuration to a 2-km resolution domain over the Colorado mountains for four individual years, reported similar seasonally-averaged (November-May) results with respect to SNOTEL ($r^2 = 0.73$ and RMSE= 92.2). Additionally, they similarly produced PRISM-relative differences in WRF of up to $\sim$300 mm which featured terrain-sensitive magnitude and sign. Despite important differences between their study and ours (i.e., domain

configuration, resolution, geographic region, our inclusion of a slab lake model), it is encouraging that similar dynamical downscaling studies over the Intermountain West produced complementary results.

Assessment of temporal validation begins in Fig. 2.4, which depicts the inter-annual time series of mean WRF and mean SNOTEL water year accumulated precipitation. There is high correlation ($r = 0.87$, $p < 0.01$) between the WRF and SNOTEL annual values but no clear evidence of a systematic sign to an overall bias in the model. Fig. 2.4b shows that percent difference between WRF and SNOTEL for each year in the simulation are bounded by approximately $+/-20\%$. The percent difference time series exhibits periodicity, and examination of its autocorrelation sequence reveals maximum lagged correlation over a period of four years, significant at $p = 0.05$ level. This temporal pattern suggests a projection of oceanic modes of variability onto the bias via storm track shifts, and we examine this at the end of section 2.3.3.

Monthly mean WRF and SNOTEL precipitation totals are shown in Fig. 2.5. WRF captures the overall seasonal trend of Wasatch precipitation with excellent monthly correlation ($r = 0.95$, $p < 0.01$), but WRF on average overestimates in December and January with a peak difference of 31.7%. The model comparably underestimates from May to September with a maximum negative difference of 27.7% in July. While we do not investigate this summertime bias in this study, we speculate that it likely arises from WRF's handling of near-surface and convective-resolving processes. Most summer precipitation over the Wasatch is from orographic con-

vection, and closer examination of summertime soil moisture, surface heat fluxes, and diurnal temperature variability may lead to clarification of this average seasonal underestimate. This seasonal tendency by WRF to produce oppositely-signed biases with respect to SNOTEL indicates that some cancellation of seasonal mean biases contributes to the overall limited magnitude of the annual bias as seen in Fig. 2.4.

A histogram of daily differences (WRF - SNOTEL) averaged across all sites is presented in Fig. 2.6. The histogram shape for all cold season days for all 25 water years (3781 days represented by grey bars in Fig. 2.6) is non-normal with a very narrow, near-zero peak, indicating the skill of the model in generally minimizing daily bias with respect to SNOTEL. The interquartile range of this distribution is also extremely narrow (-1.1 mm to 0.5 mm). The mean daily difference is positive (0.5 mm) while the median is negative (-0.3 mm). A noteworthy right tail implies the frequency of high-magnitude over-predicted days, a feature which persists when restricting to days when both WRF and SNOTEL report at least 2.54 mm (pale yellow bars in Fig. 2.6). When constrained to just these 973 days (26% of all cold season days), the mean daily difference shifts to 3.2 mm and the upper quartile becomes 6.1 mm. While such an adjustment to the distribution is not surprising (WRF-SNOTEL differences are minimized during low-precipitation days), the right shift of the daily bias distribution is important as it highlights the model's systematic tendency to over-predict cold season precipitation totals on days when measurable precipitation is both observed by SNOTEL and forecast by WRF.

To further illustrate the precipitation-bias relationship, we present a scatter plot

of daily bias versus WRF precipitation (Fig. 2.7a) and daily bias versus SNOTEL precipitation (Fig. 2.7b). Daily WRF precipitation totals correlate moderately with daily WRF-SNOTEL bias ($r^2 = 0.56$, $p < 0.01$, RMSE = 2.8 mm) thus accounting for roughly half of the variance in the daily WRF-SNOTEL bias for all simulated cold season days. We might anticipate some correlation in both panels of Fig. 2.7 because bias is by definition bounded from above (below) by the dashed line in Fig. 2.7a (Fig. 2.7b). From these scatter plots, we see that relatively large negative bias days (below bottom gray line in Fig. 2.7a-b) have low WRF precipitation (5.2 mm), yet they are relatively wet days on average as measured by SNOTEL (12.5 mm). Likewise, positive bias days tend to be associated with high WRF precipitation (blue bar, Fig. 2.7a), yet these are relatively dry days according to SNOTEL (blue bar, Fig. 2.7b). In other words, large positive and negative bias days are characteristically "wet", but only in one of WRF or SNOTEL.

As illustrated in this subsection, the model performs well overall both in terms of the temporal variability and spatial distribution of precipitation. SNOTEL undercatch (described in section 2.2.2) may explain some of WRF's systematic overprediction tendency in the predominately snowy winter precipitation regime, especially considering that gauge-height wind speeds of 4 m s^{-1} can result in undercatch of ∼30% (Yang et al., 1998). Additionally, some of WRF's errors may arise from biases with respect to the forcing reanalysis (CFSR) or errors in the CFSR data itself. The latter possibility is a problem not explicitly investigated in this study, and studies have highlighted the relative accuracy and usefulness of CFSR with respect

to other reanalysis data products (Ebisuzaki and Zhang, 2011; Hofer et al., 2012; Kim et al., 2012; Bao and Zhang, 2013; Lee and Biasutti, 2014; Sharp et al., 2015, among others). Additionally, WRF's internal processes responsible for resolving microphysics and land-atmosphere interactions may be systematically contributing to winter precipitation errors. However, our WRF configuration was specifically chosen because of its proven effectiveness in validating with respect to SNOTEL over complex Intermountain West terrain at high resolutions (Ikeda et al., 2010; Liu et al., 2011; McMillen and Steenburgh, 2014). We now turn attention to characterizing the Wasatch cold season precipitation bias in terms of the large-scale flow, highlighting the potential importance of CFSR-relative biases.

2.3.2 Synoptic Influence on Precipitation Bias

To investigate the potential influence of synoptic flow regimes on WRF's precipitation bias, we identify wet (dry) bias cold season days for which WRF over- (under-) predicted precipitation with respect to the SNOTEL regional average by at least 5 mm. As we examine these wet- and dry-bias tails, we can evaluate the observed and simulated large-scale patterns that influenced the inner domain's precipitation output because we nest higher-resolution, smaller geographic domains within lower-resolution, larger geographic domains. At the outermost (36-km resolution) domain (d01), the longwave pattern is visible, and approaching storms can be identified as they make landfall and interact with key upstream features like coastal mountain ranges. Via the nested configuration, d01 provides the boundary conditions for the

middle (12-km resolution) domain (d02) which then provides boundary conditions for the inner (4-km resolution) domain (d03).

Fig. 2.8 depicts d01 700 hectopascal (hPa) geopotential height (GPH) and specific humidity (q) fields associated with wet-bias and dry-bias days. As noted previously, the SNOTEL day runs from 08 UTC to 08 UTC and is the 24-hr period on which WRF-SNOTEL calculations are based. We can thus depict the 24-hr evolution of d01 variables from 00 UTC prior to the SNOTEL day's beginning ($00Z_{day\text{-}1}$, left column of Fig. 2.8) and at 00 UTC 16 hours into the SNOTEL day ($00Z_{day0}$, right column of Fig. 2.8). Fig. 2.8a-b depict total mean 700 hPa GPH and q fields for wet-bias days, and Fig. 2.8c-d depict the anomalies of those same variables (mean of wet-bias cold season days minus mean of all cold season days). From this figure, we see wet-bias days result from the intrusion of a strong moisture plume which follows a quasi-zonal longwave trough-ridge couplet over the western US. The anomalies noticeably feature a deep low pressure center near the US/Canada border which moves due east over the 24-hr period and guides anomalously high moisture through the Great Basin. This mean wet-bias pattern emulates closely the optimal conditions for the intrusion into Utah of a narrow corridor of vigorous moisture transport known as the atmospheric river (AR). While we do not objectively determine whether individual storms met AR criteria, the mean 700 hPa GPH and q patterns in Fig. 2.8a-b closely resemble AR climatology (Rutz et al., 2013). Fig. 2.8e-h (as in a-d but for dry-bias days) in contrast depict a more meridional (large north-south latitudinal extent) pattern of troughing over the coastal US which

delivers anomalously dry air into the northwest US behind modestly moist air feeding from farther south over the Pacific. While we cannot necessarily identify these mean regimes as archetypes of distinct storm track variations due to their averaging over large samples of individual days, their contrasts are noteworthy and suggest that characteristic large-scale conditions strongly influence the sign of precipitation bias in high-resolution simulation of Wasatch Mountain precipitation.

To further explore the distinction between the wet-bias and dry-bias samples, we produced composite 48-hr time series for several d03 parameters centered on 12 UTC (Fig. 2.9). Each hour represents the 700 hPa hourly mean of all sampled 48-hr periods at seventy d03 grid points running north-south along the spine of the Wasatch Mountains within the red-outlined region in Fig. 2.1b. During the SNOTEL day (bounded by the red vertical lines in Fig. 2.9), wet-bias days (blue curves and circles) exhibit warmer, moister air intersecting Wasatch topography with stronger mean wind speeds leading to stronger moisture fluxes, vertical velocities and higher precipitation rates than dry-bias days (brown curves and circles). For the wet-bias days, mean hourly wind direction follows a characteristic trough passage shift from increasing southwesterly followed by veering towards northwesterly. Dry-bias wind directions reflect a more southwesterly profile in the day prior with a gradual but larger total wind direction change than wet-bias days. However, during the SNOTEL day, the wind direction profile between the two sets is very similar, while wind speeds and moisture fluxes differ significantly at almost all hours. Additionally, for hourly precipitation rate, moisture, temperature, and vertical velocity, all hours in

the SNOTEL day feature statistically significant differences between wet-bias and dry-bias means (indicated by filled circles).

Most importantly, distinct noteworthy biases exist between WRF and CFSR for each case (brown and blue diamonds in Fig. 2.9b-e). Wet-bias days feature excellent agreement for moisture and wind direction (Fig. 2.9b,d), but WRF over-estimates wind speed at all hours (Fig. 2.9e). For dry-bias days, WRF underestimates moisture at all hours (Fig. 2.9b) but has good agreement in wind direction and speed (Fig. 2.9b,d). Both wet and dry-bias days have a similar cold temperature bias (Fig. 2.9c). The analysis in Fig. 2.9 further distinguishes the synoptic narratives and atmospheric conditions for wet-bias versus dry-bias days and complements the mean synoptic patterns in Fig. 2.8, particularly highlighting each case's important CFSR-relative bias over the Wasatch Mountains.

Table 2.1 summarizes the extent to which large positive and negative Wasatch precipitation biases correlate with various atmospheric quantities in WRF, now considering all simulated cold season days. As discussed above, WRF's daily precipitation total itself features high correlation ($r = 0.75$) with the model's precipitation bias, and while not a true independent variable, precipitation amount serves as the most significant predictor of daily precipitation bias with respect to SNOTEL. The only other variable that accounts for at least 25% of the variance in daily precipitation bias ($r = 0.50$) is 700 hPa zonal moisture flux (zonal component of the wind multiplied by q), indicating a relationship between WRF's large positive biases and strong orographically-forced precipitation as moisture-laden zonal flow

encounters the meridionally-oriented Wasatch Mountains. We might anticipate that much of the correlation between each parameter and the bias can be accounted for its shared correlation with precipitation amount. We confirmed this by calculating the correlation between each variable and the residuals remaining from a regression of precipitation onto the bias. The extremely low resultant correlations ($r < 0.05$ with the exception of air temperature's $r = 0.18$) emphasize the shared correlation between these parameters and precipitation amount, minimizing their explanatory power with respect to bias variability. These results indicate that no key WRF variable significantly correlates with daily bias independent of precipitation production, further highlighting the role of CFSR-relative biases in generating precipitation errors.

Motivated by the composite analyses above, we further explore why these distinct synoptic regimes result in wet and dry biases. We begin by observing that, for 00 UTC on all cold season days (Fig. 2.10a-c), WRF exhibits a small average overall dry (0-0.25 g/kg) and cold (1-2°C) bias and positive GPH bias (0-10 m) with respect to CFSR across the Great Basin (recall that CFSR provided WRF's boundary conditions). However, the influx of high moisture and warm temperatures associated with the composite storm regime during positive precipitation bias days partially offsets these mean WRF-CFSR biases (Fig. 2.10d-e). This near-zero difference between WRF and CFSR indicates that the boundary conditions feeding d03 on wet-bias days closely agrees with observations. The GPH bias, however, is inflated and features a north-south gradient with zero-line crossing the Wasatch region (Fig.

2.10f). This pattern suggests that WRF exaggerates the depth of the low passing to the north leading to cross-Wasatch wind speed bias illustrated in Fig. 2.9e. This GPH bias-driven wind error may cause over-production of orographically-enhanced precipitation, and, combined with well-documented SNOTEL undercatch, likely explains the wet bias days.

Days with negative precipitation bias (Fig. 2.10g-i), in contrast, exhibit stronger-than-average dry biases with respect to CFSR (0.25-0.75 g/kg) across the Great Basin, with the largest domain-wide biases (up to 1 g/kg) occurring over mountain ranges, including the Wasatch. One possible explanation for this enhanced dry bias across the Great Basin stems from the composite analyses in Fig. 2.8. Strong southwesterly flow perpendicular to the Sierra Nevada Mountains of southern California is indicated upstream from the Wasatch on dry-bias days in both Fig. 2.8g-h, and exaggeration of precipitation over those mountains may contribute to the dry bias seen in moisture fields downstream (brown shading, Fig. 2.10e). Dry-bias days are thus explained in part by synoptic flows that enhance WRF's overall low-humidity bias, possibly by exaggerated upstream orographic precipitation.

It should be noted that instances of close agreement between WRF and CFSR do not rule out the possibility that errors in CFSR contribute to the mean precipitation bias. However, assuming that CFSR closely approximates the true state of the atmosphere, this analysis suggests that part of the seasonal wet bias may arise from overestimation of the GPH gradient perpendicular to the Wasatch during northern passage of storms that produce modest observed precipitation. Dry-bias days appear

to partly result from exaggeration of upstream moisture removal due to the more southwesterly flow ahead of higher observed storm precipitation totals.

2.3.3 Oceanic Influence on Bias

The final element of our bias evaluation investigates the potential relationship between Pacific sea surface temperature (SST) variability and the Wasatch seasonal precipitation bias. Tropical Pacific SST variability is known to impact extratropical wave propagation (Hoerling and Kumar, 2002; Seager et al., 2003; Orlanski, 2005). Recent studies have sought to describe the processes that force these mean flow anomalies, including Harnik et al. (2010), who decomposed the role of eddy heat and momentum fluxes driven by tropical SST anomalies in altering Pacific long-wave geometry. Considering the relationship between WRF's synoptic regime characteristics and WRF-SNOTEL differences over the Wasatch, tropical SST variability's influence on eddy pathway into the western US may relate to WRF's wintertime precipitation bias. Fig. 2.11 depicts correlation coefficients for mean cold season SST anomalies across the Pacific with the corresponding year's Wasatch Mountain accumulated seasonal precipitation bias produced by WRF. Here we correlated each of the 25 water year's accumulated cold season precipitation difference between WRF and SNOTEL with the mean cold season SST anomaly at each point across the pacific for that corresponding year. The observational SST data used (HadISST) are reconstructed gridded monthly data from in situ and satellite observations obtained from the Met Office Hadley Centre (Rayner et al., 2003). The equatorial dipole over the tropical

Pacific aligns with the characteristic SST anomaly pattern associated with the El Niño-Southern Oscillation (ENSO). The moderate negative correlation ($r = -0.5$) suggests a relationship between La Niña winters (cold phase of ENSO) and positive cold season WRF precipitation bias over the Wasatch. In the Niño 3.4 region (white box, Fig. 2.11) mean SST correlates negatively with both the number of cold season wet-bias days ($r = -0.55$, $p < 0.01$) and the total cold season difference between WRF and SNOTEL precipitation ($r = -0.48$, $p = 0.01$). Although we did not perform a storm-by-storm decomposition of the full 25-yr simulation, the number of cold season wet-bias days here provides a reasonable proxy for wet-bias storm system passage. One study that more explicitly clarifies this relationship is (Seager et al., 2010) wherein systematic changes in the eastern Pacific storm track arise during different ENSO phases. During El Niño winters, the storm track is displaced southward, while the La Niña storm track exhibits a dominant northeast-trending pathway for transient eddy propagation. This La Niña pathway, which correlates positively with Wasatch wintertime precipitation bias in our simulations, drives storm systems towards the Pacific Northwest of the US, a pattern which coincides with Fig. 2.8 (top half). This analysis suggests that tropical Pacific SST-driven modifications in the storm track may guide storm system orientation preferentially toward more northern tracks associated with exaggerated cross-Wasatch GPH gradients and wind speeds. The previously-noted 4-yr autocorrelation in water year precipitation biases complements this analysis considering its overlap with the ENSO period. Further analysis is needed to fully understand the role of natural variability such as ENSO

and its relationship with WRF's Intermountain West precipitation bias.

2.4 Discussion and Conclusions

This study demonstrates the utility of WRF-downscaling methodology to retrospectively simulate historical precipitation over the Wasatch Mountains. The model largely captured the spatial and temporal pattern of seasonal and inter-annual precipitation, with maximum departure from SNOTEL observations generally during those days and months that featured the highest precipitation totals. The spread and central tendency of the daily WRF-SNOTEL precipitation differences, along with WRF and SNOTEL's strong seasonal correlations, gives confidence in the overall skill of this modeling configuration. Considering SNOTEL measurement errors from wind-driven undercatch, the model appears to be generally effective in simulating the processes that lead to precipitation over the Wasatch Mountains. Future analysis of the performance of other key hydroclimate elements such as snowpack and runoff is warranted. We conducted a brief comparison between WRF's snow water equivalent (SWE) output and SNOTEL (not depicted), and the model captures the overall spatial and temporal pattern of SWE accumulation and ablation, but a consistent underestimate of $\sim$20% exists. This result is consistent with other studies of similar WRF configurations, and the Noah LSM's treatment of snow and canopy effects is cited as a possible explanation (Rasmussen et al., 2011a, 2014).

More significant daily and storm-specific over- and under-prediction by WRF relates to mean atmospheric properties as follows: WRF over-predicts cold season

Wasatch precipitation during relatively vigorous, warm, moist storm systems with strong geopotential height gradients extending from a deep low-pressure center which follows a more zonal, northern track. WRF under-predicts more southern-tracking storms with southwesterly flow crossing the High Sierras upstream. The composite differences between the mean characteristics of these two regimes is statistically significant when analyzed hourly. Dry-bias days are explained in part by synoptic flows that enhance WRF's overall cool, low-humidity bias, possibly by exaggerated upstream orographic precipitation. The wet-bias regime's synoptic characteristics tend toward near-zero WRF-CFSR temperature and humidity biases, but the pattern of enhanced GPH bias exaggerates cross-Wasatch wind speeds and possibly orographically-enhanced precipitation. Although we focused on the Wasatch here, we speculate general applicability of the finding that precipitation bias fluctuates with synoptic regimes that modulate overall background humidity, temperature, and GPH biases. Details on sign and the pathways of synoptic adjustment likely depend on the region of study (e.g., proximity to upstream topography and zonal flow orientation).

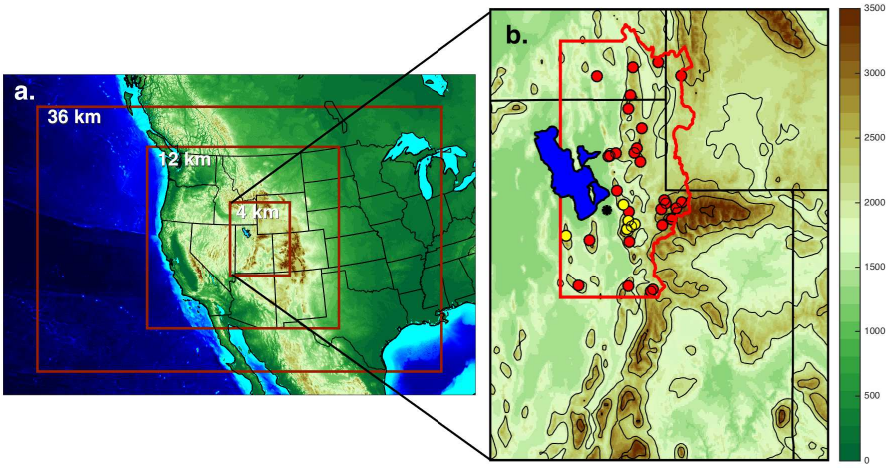

Fig. 2.1. The domains used in this study. (a) Red rectangles are boundaries of nested WRF domains with resolutions increasing from 36 km to 12 km and 4 km. (b) Innermost domain with SNOTEL subdomain outlined in red. Red filled circles indicate SNOTEL sites active for the entire period of historical simulation. Yellow filled circles are SNOTEL sites included in validation calculations starting in their first full active water year.

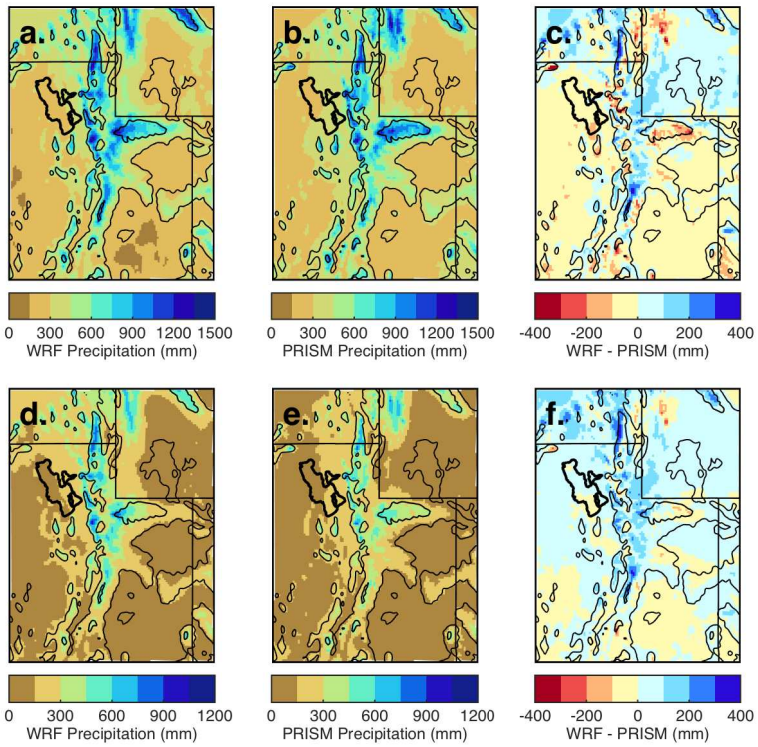

Fig. 2.2. Comparison of WRF and PRISM climatology. (a-c) Water year precipitation climatology from WRF, PRISM, and difference (WRF−PRISM). (d-f) Same as in (a-c) but for cold season climatology (1 November–31 March). Elevation is contoured at 1,000-m intervals from 2,000-5,000 m (black curves).

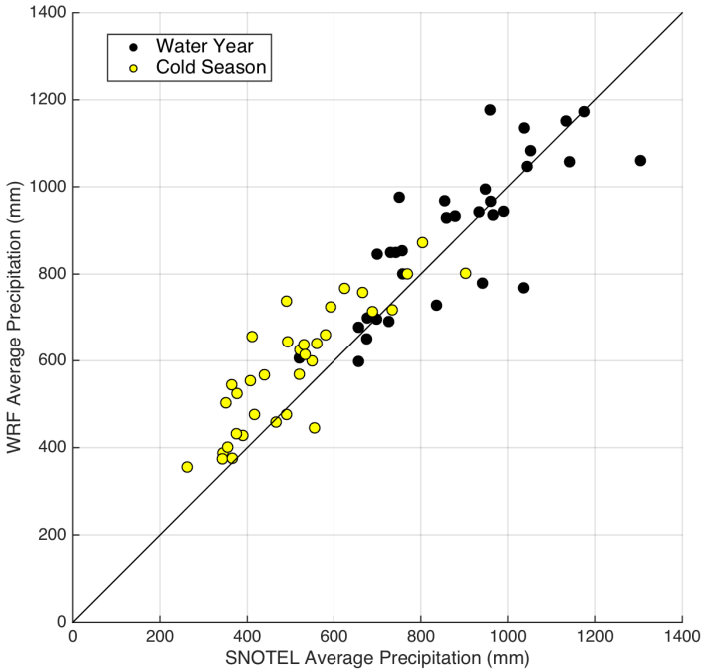

Fig. 2.3. Average SNOTEL precipitation for all simulated years compared with corresponding data from WRF. Yellow (black) filled circles represent cold season (water year) precipitation. Each point represents the average corresponding to the location of a single SNOTEL station. One-to-one line is plotted for reference.

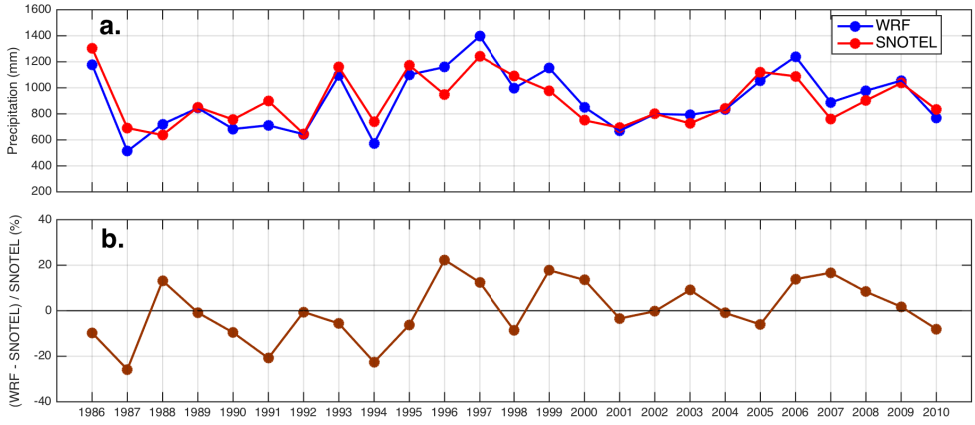

Fig. 2.4. Comparison of WRF and SNOTEL water year precipitation. (a) Annual water year precipitation for SNOTEL (red) and WRF (blue). (b) Percent difference (100∗(WRF - SNOTEL)/SNOTEL).

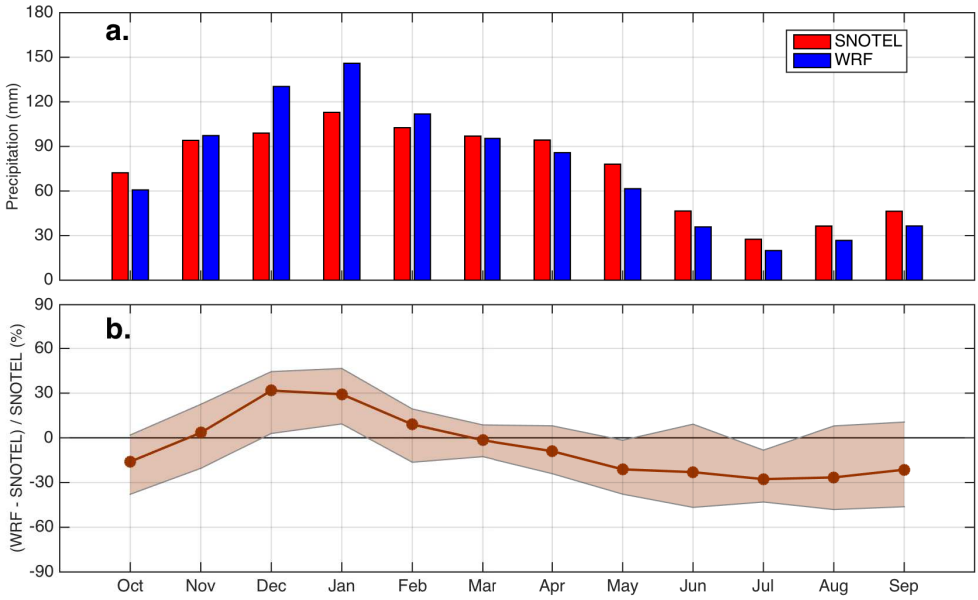

Fig. 2.5. Comparison of WRF and SNOTEL monthly precipitation climatology. (a) Seasonal cycle of precipitation climatology for SNOTEL (red) and WRF (blue). (b) Percent difference (100∗(WRF - SNOTEL)/SNOTEL) by month with brown shaded interquartile range (25^{th}-75^{th} percentiles) for the distribution of the given month's bias across all years.

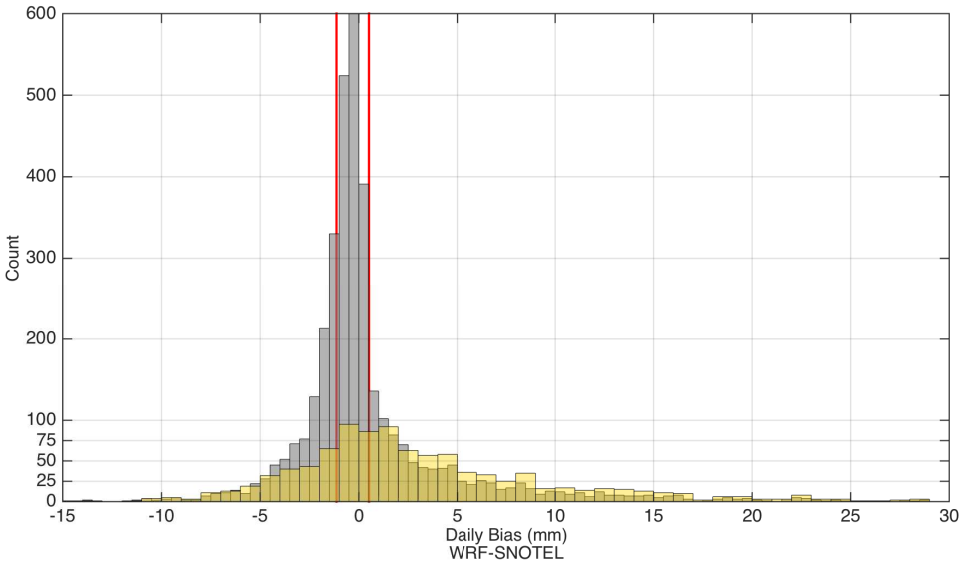

Fig. 2.6. Histogram of daily precipitation biases (WRF - SNOTEL) for all cold season days in historical simulation. Grey bars represent all cold season days with associated interquartile range bounded by red bars. The upper limit of tallest grey bar is 871 (ordinate is cropped). Pale yellow histogram represents only those days where WRF and SNOTEL both reported at least 2.54 mm (0.1 inch) of precipitation. Binning method applies Freedman-Diaconis rule (Freedman and Diaconis, 1981).

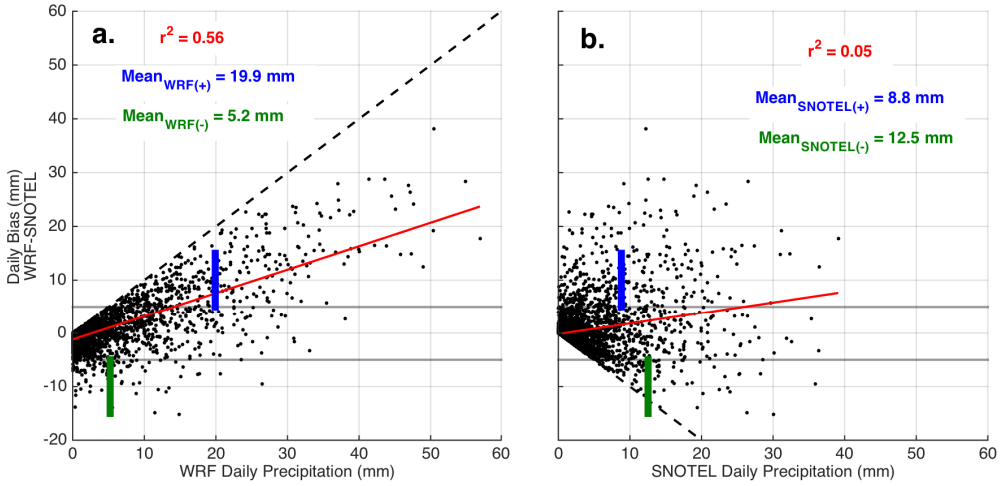

Fig. 2.7. Scatter plots and linear fits of daily cold season bias versus WRF or SNOTEL daily precipitation. (a) Scatter plot and linear fit (red line) of WRF daily precipitation bias (relative to SNOTEL) for all cold season days versus associated daily WRF precipitation. Dashed one-to-one line shows mathematical limit of bias calculation. Horizontal gray lines indicate thresholds for sampling large positive (5 mm) and negative (−5 mm) bias days for analysis in section 2.3.2. Blue (green) vertical line denotes the average WRF precipitation value for large positive (negative) biased days. (b) As in (a) but with SNOTEL observed precipitation on the abscissa.

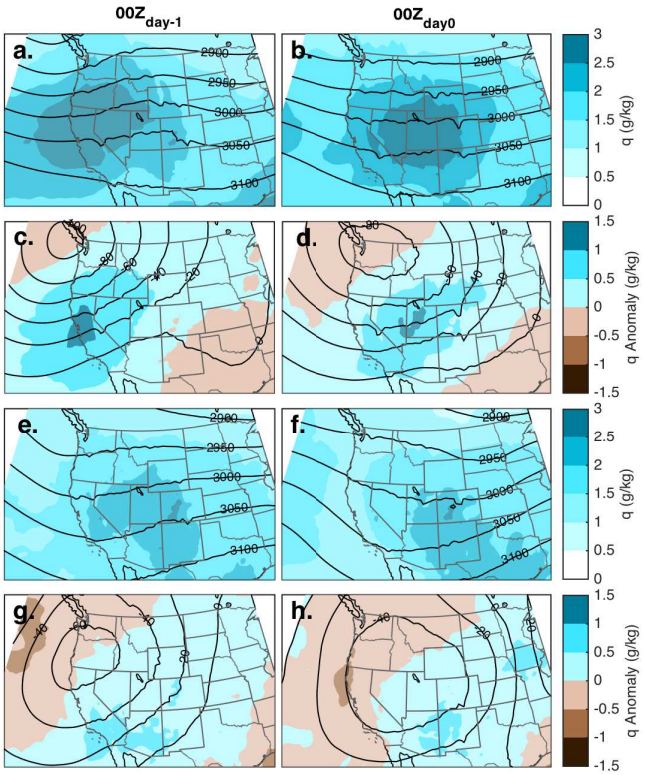

Fig. 2.8. Composites of WRF 700 hPa geopotential height (GPH) and specific humidity (q). (a-b) Mean 700 hPa q (shading) and GPH (contour) fields at 00 UTC prior to ($00Z_{day\text{-}1}$) and during ($00Z_{day0}$) days where WRF-SNOTEL difference was positive by at least 5 mm. (c-d) As in (a-b) but for 700 hPa q and GPH anomalies (mean of wet-bias cold season days minus mean of all cold season days). (e-h) As in (a-d) but for dry-bias days (i.e., WRF-SNOTEL difference was negative by at least 5 mm).

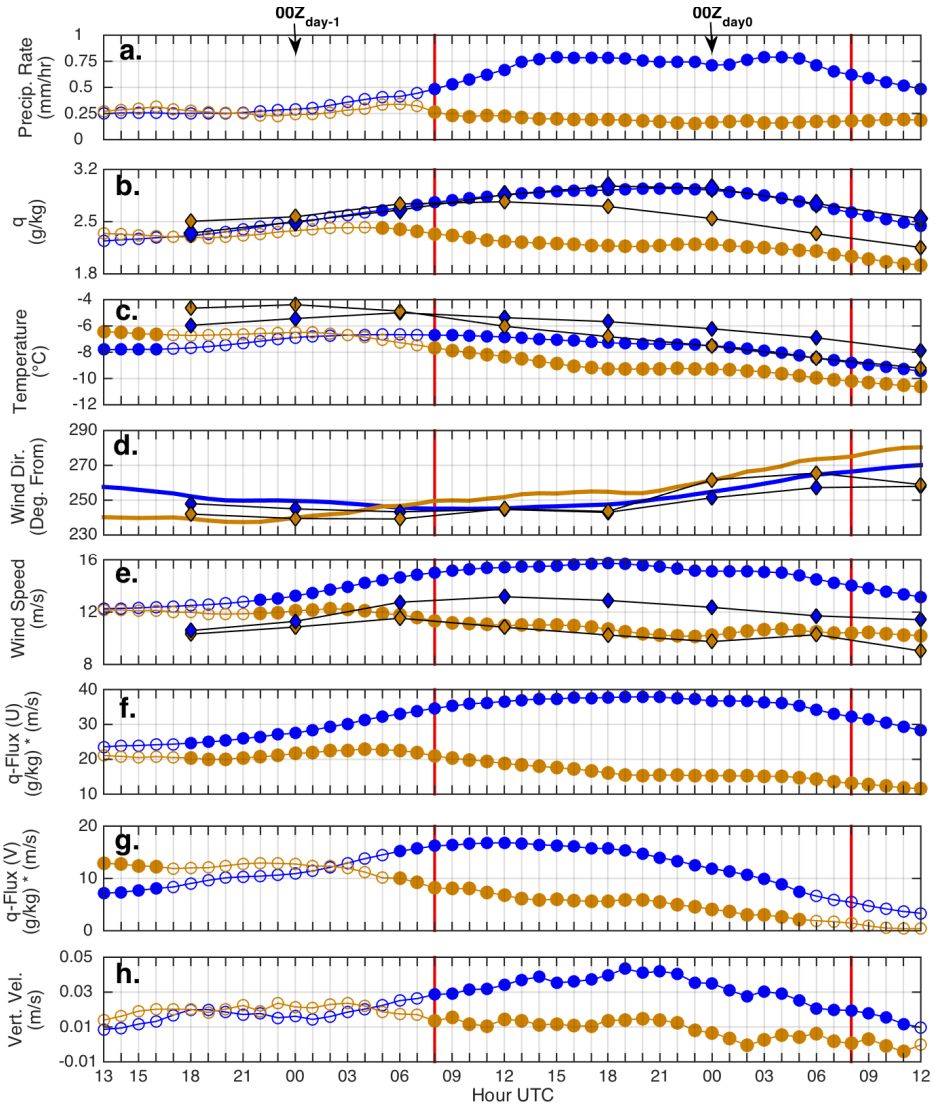

Fig. 2.9. Mean hourly composites for eight WRF variables averaged along the spine of the Wasatch Mountains within the red-outlined region in Fig. 2.1b. The composite corresponds to 48-hr periods surrounding wet-bias days (blue) and dry-bias days (brown) for daily WRF-SNOTEL differences of at least 5 mm. Filled circles indicate hours for which difference between wet-bias days' and dry-bias days' mean WRF values are statistically significant at the $p = 0.05$ level by t-test. Significance test was not performed for wind direction. (b-e) Blue (brown) filled diamonds indicate corresponding CFSR mean 6-hrly values for wet (dry) bias days. Red vertical lines bound the 08 UTC to 08 UTC day for which the WRF-SNOTEL bias was defined and calculated. $00Z_{day\text{-}1}$ and $00Z_{day0}$ are indicated along top, as in Fig. 2.8.

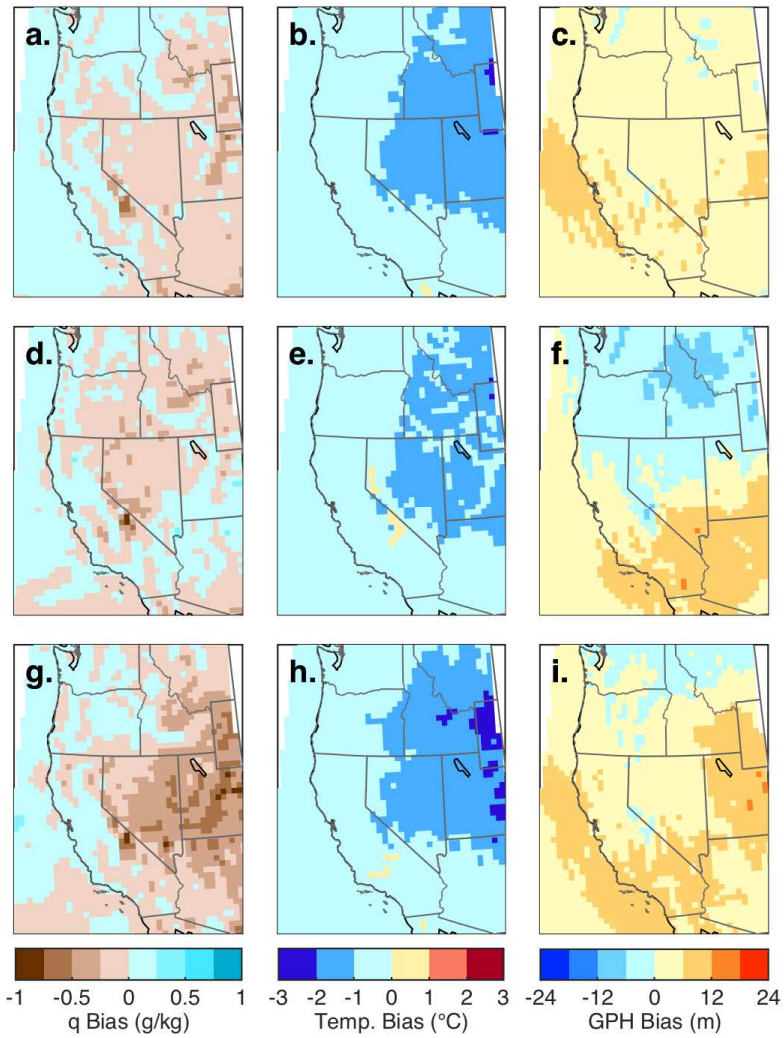

Fig. 2.10. Composites of model bias at 700 hPa (WRF minus CFSR). (a) Mean 700 hPa specific humidity bias, (b) mean 700 hPa temperature bias, and (c) mean 700 hPa geopotential height bias (WRF - CFSR) at 00 UTC on all cold season days. (d-f) Same as in (a-c) but for wet-bias days (WRF-SNOTEL difference was positive by at least 5 mm). (g-i) Same as in (a-c) but for dry-bias days (WRF-SNOTEL difference was negative by at least 5 mm).

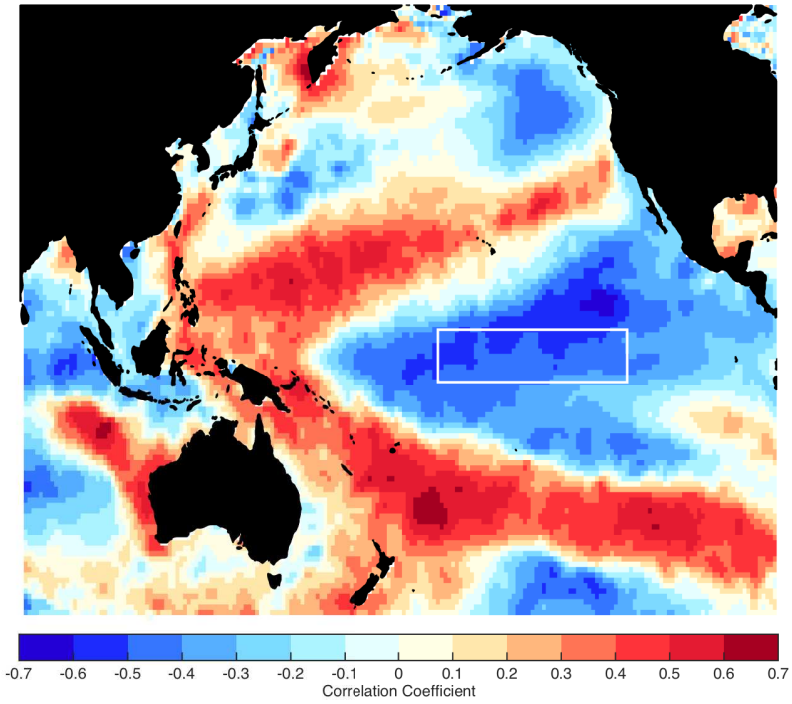

Fig. 2.11. Correlation map for mean cold season sea surface temperature and cold season WRF precipitation bias over the Wasatch Mountains for all 25 water years. White box outlines Niño 3.4 region referenced in text.

Table 2.1. Correlations between daily mean WRF parameters and daily precipitation bias (WRF - SNOTEL) for all cold season days. All correlations are significant at $p < 0.01$. Precipitation is taken from sites show in Fig. 2.1b, and all other variables are 700 hPa mean daily values along the spine of the Wasatch Mountains within the red-outlined region in Fig. 2.1b.

WRF Daily Mean Parameter	r
precipitation amount	0.75
zonal moisture flux	0.50
wind speed	0.41
vertical velocity	0.37
specific humidity	0.37
meridional moisture flux	0.25
air temperature	0.06

CHAPTER 3

WESTERN UNITED STATES SNOWPACK ANALYSIS

3.1 Introduction

The studies described in section 1.2 established a foundation for answering the crucial question of how climate change may adjust the elevation threshold above which precipitation is the main driver of snowpack variability and below which temperature is the main driver. Their varied results for this threshold suggests that other study areas may exhibit different threshold elevations. There may also be geographically-varying results for climate change-driven modifications to those thresholds. The following chapter describes an adaptation of these studies' analyses to six subregions of the western U.S. and extends this framework to assess the changing relative roles of temperature and precipitation in driving spring snowpack variability under a moderate climate change perturbation at the end of the 21st century.

An overview of the historical and pseudo-global warming simulations compared in this study are described in section 3.2.1.-3.2.2. In section 3.2.3, we describe the statistical analysis applied to characterize the snowpack variability and associated

correlations. Results and discussion are presented in section 3.3, and conclusions are summarized in section 3.4.

3.2 Data and Methods

3.2.1 WRF Historical Simulation

For this portion of the study, we analyzed monthly mean 2-m air temperature (T), SWE, and monthly accumulated precipitation (P) from the historical simulation featured in Chapter 1 (hereafter denoted $\mathrm{WRF_{Past}}$) on d02 and d03, spanning 1995-2004. Validation of $\mathrm{WRF_{Past}}$ for this section of the study was conducted on d02 against Parameter-elevation Regressions on Independent Slopes Model (PRISM) data (Daly et al., 1994, 2008). This data set is available from the PRISM Climate Group, Oregon State University (http://prism.oregonstate.edu) where we acquired monthly mean temperature and monthly precipitation data for the period of this study (1995-2004) on a 4-km grid. The results are presented in Fig. 3.1 for annual total precipitation and annual mean temperature averaged over the decade. While a weak wet bias and weak cold bias is apparent over portions of the Intermountain West, overall excellent spatial correlation exists between $\mathrm{WRF_{Past}}$ and PRISM.

Additionally, we used automated daily observations of T, P, and SWE from 29 Snow Telemetry (SNOTEL) sensors operated by the National Resources Conservation Service (NRCS) of the United States Department of Agriculture to assist in validating $\mathrm{WRF_{Past}}$ in section 3.3.

3.2.2 Pseudo-Global Warming Simulation

Future climate-driven modification of the roles of temperature and precipitation in snowpack variability is estimated using the pseudo global warming (PGW) approach (Schär et al., 1996; Kawase et al., 2009; Rasmussen et al., 2011a). This technique applies a mean monthly perturbation to initial and boundary conditions based on reanalysis fields to simulate future climate with minimal alteration of the historical sub-monthly storm track characteristics and frequency. The climate model used to calculate the perturbation was the National Center for Atmospheric Research (NCAR) Community Climate System Model, version 4 (CCSM4) (Gent et al., 2011). Our choice of this particular model follows a comparative analysis of 20 models in which CCSM4 most consistently captured observed connections between Great Basin precipitation and Pacific sea surface temperature variability (Smith et al., 2015). The monthly climate change perturbation ($\Delta\text{CCSM4}_{\text{month mean}}$) was calculated as the difference between the 10-yr monthly average SST, temperature, and relative humidity from 2085 to 2094 and the 20-yr averages for 1985 to 2004 under the medium-high emission scenario (RCP 6.0). This perturbation was then applied to the CFSR 3-hrly data for the WRF model initial and boundary conditions for 10 years of current climate (1995 to 2004) as shown below:

$$PGW = \triangle CCSM4_{\text{month mean}} + CFSR \tag{3.1}$$

From the PGW simulation (hereafter called WRF_{PGW}), monthly mean T, SWE, and monthly accumulated P were obtained for comparison with WRF_{Past}.

Fig. 3.2 depicts the mean change in surface temperature averaged over March and April ($T_{\text{Mar-Apr}}$), precipitation accumulated over October-April ($P_{\text{Oct-Apr}}$), and mean April SWE (SWE_{Apr}) for WRF_{PGW} minus WRF_{Past}. Broadly across the western U.S., $T_{\text{Mar-Apr}}$ change ranges 2-6°C, with an overall positive elevation-dependent warming signature. $P_{\text{Oct-Apr}}$ changes positively under WRF_{PGW} as well, broadly ranging 0-20% with isolated areas up to 30%. These parameters were chosen for comparison here because they are used in the statistical analysis of temperature- and precipitation-driven SWE_{Apr} variability in this study. Additionally, changes in western U.S. annual mean temperature ($\sim 2-4$°C) and annual mean accumulated precipitation (up to $\sim$ 30%) were calculated (not shown), and these results are broadly consistent with the spatial patterns and magnitude of annual mean changes in the CCSM4 RCP6.0 ensemble mean as shown by Peacock (2012) (see their Figs. 5 and 13). Additionally, a study by Pierce and Cayan (2012) in which they statistically downscaled an ensemble of climate models produced complementary end-of-century changes across western U.S. mountain ranges (see their Fig. 2). Associated losses in SWE_{Apr} are widespread, ranging 0-50%, with larger losses coinciding with the lowest elevations of mountain ranges (Fig. 3.2c). Only the very highest elevations of the Middle Rockies (MR), Sierra Nevada (SN), and eastern edge of the Wasatch (WA) exhibit small SWE gains (less than 20%). It should be noted that d02 does not fully resolve the terrain height of these mountains, a limitation of this analysis which deserves further investigation.

3.2.3 Statistical Methods

In this study, we analyzed SWE_{Apr} as a measure of western U.S.-wide late spring snowpack because peak annual SWE in the western U.S. predominately occurs from late March to mid-April (Serreze et al., 1999). Following Sospedra-Alfonso et al. (2015), we for each grid point computed the Pearson correlation between SWE_{Apr} and $T_{Mar\text{-}Apr}$ and also the Pearson correlation between SWE_{Apr} and $P_{Oct\text{-}Apr}$. Sospedra-Alfonso et al. (2015) adjusted the elevations of their $T_{Mar\text{-}Apr}$ correlations to fit a representative average atmospheric lapse rate to account for subdomain thermal heterogeneity. We did not include any adjustments to elevation here because we found that they would only minimally impact the variance structure of our data, and the need for climate state-dependent adjustments (past versus future) would confound interpretation of climate-driven changes in threshold elevations.

For each mountain subdomain (red polygons in Fig. 3.3b), we analyzed only those grid points achieving at least the 40^{th} percentile of that subdomain's mean SWE_{Apr} (P_{40}, summarized in Table 3.1) for the majority of the simulated water years. This criterion led to analysis of approximately 50% of each subdomain's grid points ("P_{40} Area" in Table 3.1).

3.3 Results

We begin with a detailed analysis of the Wasatch subdomain (WA, Fig. 3.3c) because we have 4-km resolution data available for this region from simulation domain d03. Fig. 3.4 depicts the correlation coefficients for SWE_{Apr} versus both

$T_{\text{Mar-Apr}}$ (r_T) and $P_{\text{Oct-Apr}}$ (r_P) for both WRF_{Past} (Fig. 3.4a) and WRF_{PGW} (Fig. 3.4b). A linear least squares regression for the correlation coefficients versus elevation for $T_{\text{Mar-Apr}}$ is also depicted, indicating weakening of the negative correlation with elevation ($r^2 = 0.79$). Studies by Sospedra-Alfonso et al. (2015) and Morán-Tejeda et al. (2013) found that the positive correlation between P and SWE increases linearly with elevation, but the high density and large elevation range of our model data in Fig. 3.4a suggests a curvilinear pattern for $P_{\text{Oct-Apr}}$ correlations. We fit a logarithmic function with high-elevation asymptote $r_P = 1$

$$r_P = 1 - e^{-a_1(H-a_2)}, \tag{3.2}$$

where H is the elevation of the grid points, yielding $r^2 = 0.52$ for $a_1 = 0.0017$ and $a_2 = 802.4$. A threshold elevation separating where temperature and precipitation drive snowpack variability is inferred from the intersection point of the logarithmic fit to r_P and linear fit to r_T. For WRF_{Past}, this threshold is 1946 ± 20 m, with the range of uncertainty estimated by taking the maximum departure from this intersection given by the 95% confidence bounds on the fit parameters (dashed black curves in Fig. 3.4a). Note that these bounds assume that the correlations from the 4-km grid are spatially independent, and restriction to fewer degrees of freedom would inflate these bounds (i.e., using the 12-km data from domain d02 for the Wasatch subdomain would result in bounds ± 71 m). This elevation threshold rises to 2263 ± 25 m under WRF_{PGW} climate change (Fig. 3.4b), a change of 317 m that indicates the expanded range of elevations for which spring SWE variability responds more strongly to spring temperature variations than to precipitation in WRF_{PGW}. In Fig. 3.4a, we also

plot the $T_{Mar\text{-}Apr}$ and $P_{Oct\text{-}Apr}$ correlations with SWE_{Apr} as given by 29 SNOTEL stations across the Wasatch subdomain (locations indicated by red filled circles in Fig. 3.3c; locations detailed in Table 3.2). This SNOTEL analysis follows that which Sospedra-Alfonso et al. (2015) conducted in the Northern Rockies (with the exception of their adjustment to effective elevations) and confirms that WRF_{Past} realistically captures the overall pattern of observed covariation. We note that simulated r_P tends to be larger than observed, especially at the highest elevations, and the range of simulated r_T is smaller than observed at most elevations.

A Snowpack Sensitivity Index ("SSI", as in Fig. 3c of (Sospedra-Alfonso et al., 2015)), defined as the sum of r_T and r_P, is depicted in Fig. 3.4c-d for WRF_{Past} and WRF_{PGW}. The predominately positive SSI in WRF_{Past} across the Wasatch subdomain (blue shading, Fig. 3.4c) indicates an overall precipitation-driven snowpack variability in the historical climate. Relatively sparse ares of negative SSI indicate crossover to temperature-driven snowpack at lower elevations (below ∼1946 m). In WRF_{PGW}, an increased fraction of the subdomain features negative SSI (Fig. 3.4d), reflecting the encroachment of temperature-driven snowpack variability to higher elevations across the Wasatch. This overtaking of more spatial area by temperature-driven SWE variability coincides with the rise of the threshold elevation below which temperature drives SWE variability (i.e., the change from Fig. 3.4a to 3.4b).

The analysis illustrated in Fig. 3.4 was repeated for five other subdomains of the western U.S. (red polygons in Fig. 3.3b), and the results are summarized in

Fig. 3.5 and Table 3.1. We use the 4-km data available on the d03 domain for the Colorado Rockies (top row of Fig. 3.5), and we use the data from the d02 domain for the other four subregions (rows 2-5 in Fig. 3.5), noting that 4-km data on d03 and 12-km data on d02 yield comparable results (e.g., Fig. 3.6a-b versus Fig. 3.4c-d). For all subdomains analyzed, the intersection of the linear and logarithmic fits shifts to higher elevations for $\mathrm{WRF_{PGW}}$, as summarized in Table 3.1. Both under $\mathrm{WRF_{Past}}$ and $\mathrm{WRF_{PGW}}$, the threshold elevation varies across the western U.S., ranging $1574-2119$ m in the past climate and $1858-2387$ m in the future climate. For the Northern Rockies, the $\mathrm{WRF_{Past}}$ threshold is 1595 ± 38 m, a result which closely matches the 1578 ± 76 m reported by Sospedra-Alfonso et al. (2015). Under the prescribed climate change, a range of threshold elevation changes occurred across the western U.S. (column 4 of Table 3.1), with a mean of 317 m, median of 311 m, a maximum of 447 m (over the Middle Rockies), and a minimum of 239 m (over the Colorado Rockies). The spatial impact of these changes is notably different across subdomains. For example, the 330 m rise in threshold elevation over the Washington Cascades leads to a consumption of virtually all analyzed elevations up to mountain peak height by temperature-driven SWE variability (Fig. 3.5g-h). For the Colorado and Middle Rockies, virtually all analyzed elevations were driven by precipitation variability in the past, and future increases in threshold elevations expose the lowest analyzed elevation tier to temperature-driven SWE variability under future climate (Fig. 3.5a-d).

To further illustrate these western U.S.-wide modifications under PGW, Fig. 3.6

shows the d02-wide Snowpack Sensitivity Index (SSI; $r_T + r_P$) for $\mathrm{WRF_{Past}}$ and $\mathrm{WRF_{PGW}}$, and the SSI change ($\mathrm{WRF_{PGW}}$ - $\mathrm{WRF_{Past}}$). For each of the mountain subdomains analyzed, there is an overall decrease in SSI under moderate climate change (blue shading within black polygons in Fig. 3.6c). This encroachment of lower SSI values across the western U.S. reflects the increasing control of spring temperature variability on April mean SWE variability. The associated increase in threshold elevations quantified in Table 3.1 indicates that more of the mountainous area of the western U.S. becomes subject to temperature-driven rather than precipitation-driven snowpack variability. In general, the decrease in SSI has a maximum of -0.2 to -0.4, but there are isolated regions up to -0.8, particularly in the Northern, Middle, and Southern Rockies.

3.4 Conclusions

We have shown that for six mountainous regions in the western U.S., the dependence of April mean SWE on precipitation and temperature exhibits notable spatial and elevational variation. The threshold elevation above which precipitation is the main driver of SWE was found to rise by 239 to 447 m under a moderate climate change perturbation, and this large range of modifications may stem from the complex dependencies of spring SWE on local precipitation regimes, topography, and the partitioning of rain and snow in wintertime precipitation under a changing climate. These varying threshold changes imply domain-specific ecological and hydrologic impacts, particularly considering the variety of elevation ranges vulnerable to

these changes. For example, while some mountain ranges have their middle elevation tier encroached upon by more temperature-driven SWE variability (Sierra Nevada, Northern Rockies, Wasatch), others have their top tier (Washington Cascades) or lowest tier (Middle and Colorado Rockies) overtaken by temperature effects. Each mountain subdomain's individual susceptibility to this rising threshold projects onto regionally-specific water balance and ecosystem sensitivities, motivating further detailed investigation. However, our results overwhelmingly indicate an enhanced vulnerability of the snowpack to temperature variability in a changing climate.

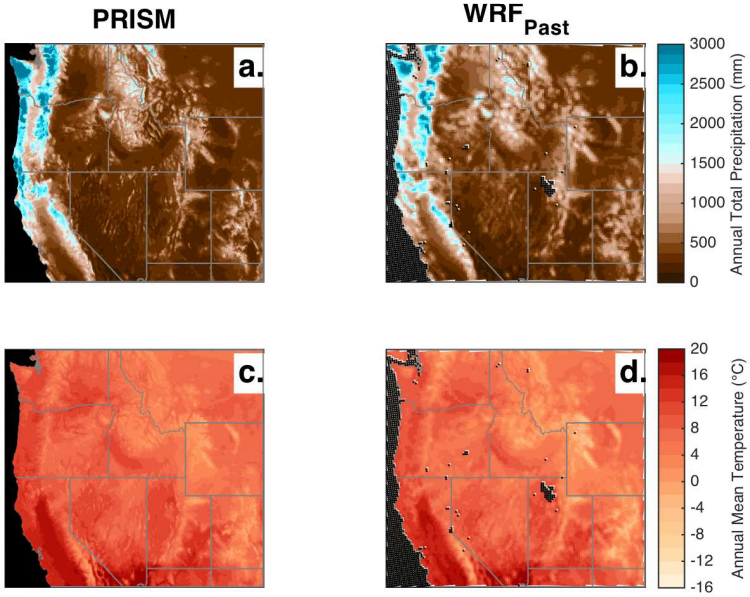

Fig. 3.1. Comparison of PRISM and WRF climatologies of annual precipitation and temperature. (a-b) Climatology of annual accumulated precipitation (1995-2004) from PRISM (4-km horizontal resolution) and $\mathrm{WRF}_{\mathrm{Past}}$ (12-km horizontal resolution). (c-d) As in (a-b) but for annual mean temperature.

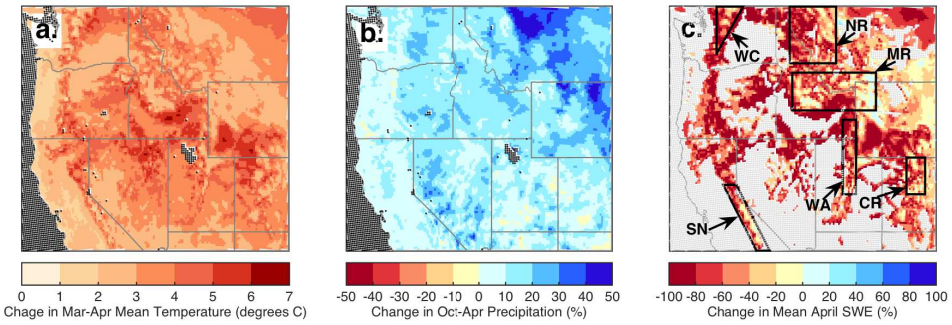

Fig. 3.2. Average change (WRF_{PGW}-WRF_{Past}) in (a) March-April mean surface temperature, (b) October-April accumulated precipitation, and (c) April mean SWE. In (c), gray shading masks the grid points not achieving at least 1 mm of April mean SWE for the majority of simulated years, and the black polygons indicate the mountain subdomains used in statistical analysis described in section 2.3 (WC: Washington Cascades; SN: Sierra Nevada; NR: Northern Rockies; MR: Middle Rockies; WA: Wasatch; CR: Colorado Rockies).

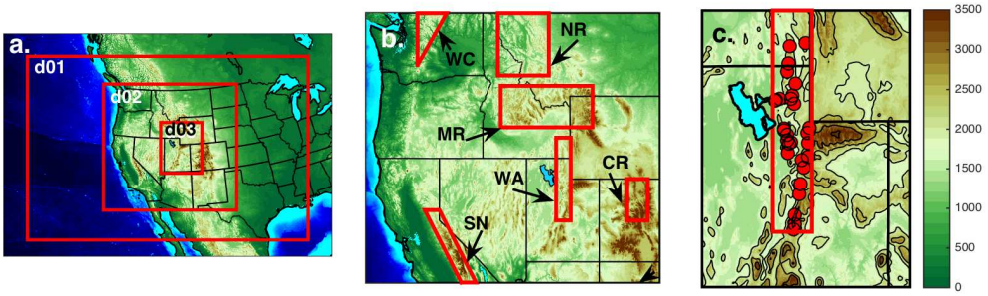

Fig. 3.3. Study area and domains used in this study. (a) Red rectangles are boundaries of nested WRF domains with horizontal resolutions increasing from 36 km (d01) to 12 km (d02) to 4 km (d03). (b) Red polygons indicating the mountain subdomains used in statistical analysis described in section 2.3 (WC: Washington Cascades; SN: Sierra Nevada; NR: Northern Rockies; MR: Middle Rockies; WA: Wasatch; CR: Colorado Rockies). (c) Wasatch sub-domain outlined in red. Red filled circles indicate SNOTEL sites used for Wasatch-specific analysis in Fig. 3.4a (locations detailed in Table 3.2).

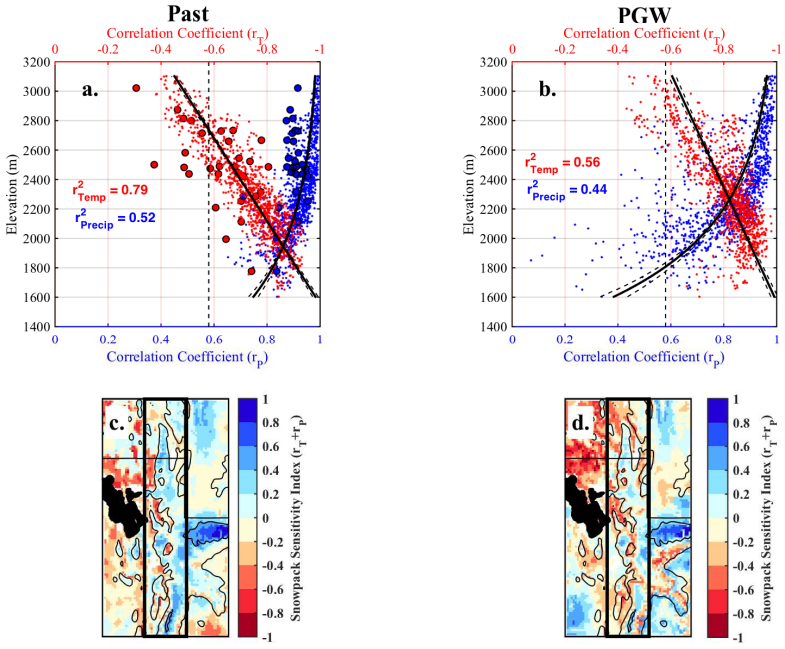

Fig. 3.4. Results of statistical analysis for the Wasatch subdomain. (a) Pearson correlations between $\mathrm{SWE_{Apr}}$ and $\mathrm{T_{Mar\text{-}Apr}}$ (small red dots), and between $\mathrm{SWE_{Apr}}$ and $\mathrm{P_{Oct\text{-}Apr}}$ (small blue dots), as a function of elevation for $\mathrm{WRF_{Past}}$ over the Wasatch subdomain (defined in Fig. 3.3c). The solid black line and curve indicate linear (r_T) and logarithmic (r_P) fits, and the 95% confidence bounds for each are indicated by dashed black curves. Larger filled red and blue circles are SNOTEL correlations at sites indicated in Fig. 3.3c. Vertical dashed line ($|r| = 0.58$) indicates the threshold above which correlation absolute values are statistically significant ($p < 0.05$). (b) As in (a) but for $\mathrm{WRF_{PGW}}$, excluding SNOTEL analysis. (c) Sum of correlations ($r_T + r_P$) for $\mathrm{WRF_{Past}}$ with bold black border indicating the Wasatch subdomain. (d) As in (c) but for $\mathrm{WRF_{PGW}}$.

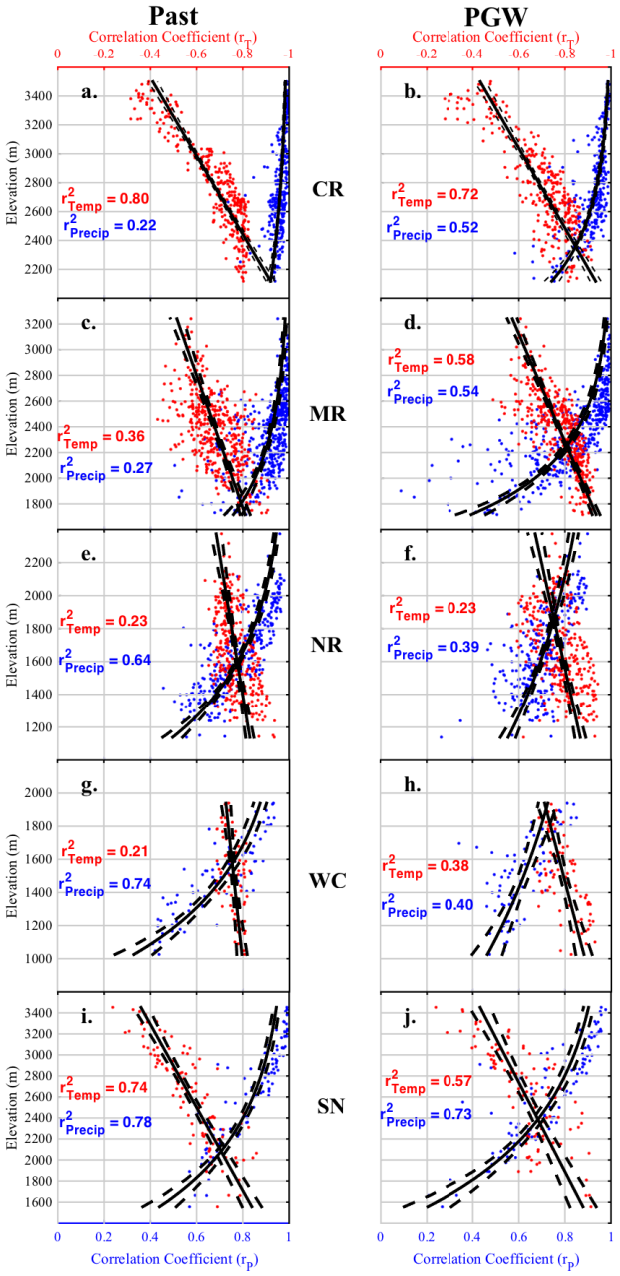

Fig. 3.5. Results of statistical analysis for five mountainous subdomains of the western United States. (a-b) As in Fig. 3.4a-b but for the Colorado Rockies, excluding SNOTEL analysis. (c-j) As in (a-b) but for mountain subdomain indicated between columns (MR: Middle Rockies; NR: Northern Rockies; WC: Washington Cascades; SN: Sierra Nevada).

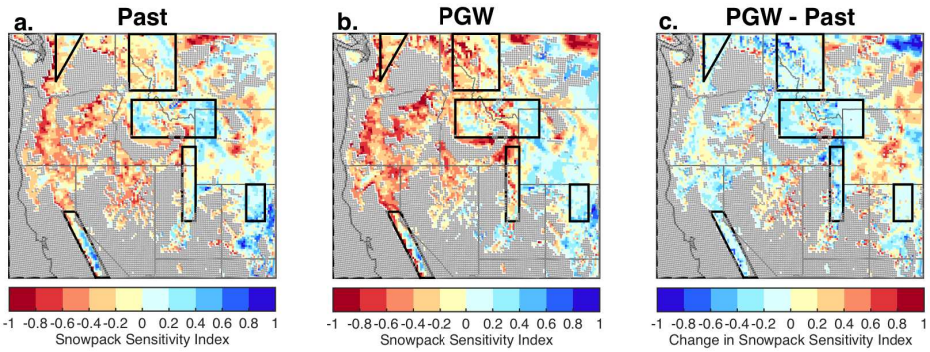

Fig. 3.6. Snowpack sensitivity index (SSI; $r_T + r_P$) for (a) $\mathrm{WRF}_{\mathrm{Past}}$, with mountain subdomains indicated by black polygons. (b) As in (a) but for $\mathrm{WRF}_{\mathrm{PGW}}$. (c) SSI in $\mathrm{WRF}_{\mathrm{PGW}}$ minus SSI in $\mathrm{WRF}_{\mathrm{Past}}$.

Table 3.1. Threshold elevations above which precipitation is the main driver of snowpack variability and below which temperature is the main driver. Results are shown for a historical simulation spanning 1995-2004 ($\text{Threshold}_{\text{Past}}$), a simulation perturbed with future climate spanning 2085-2094 ($\text{Threshold}_{\text{PGW}}$), and the change $\text{Threshold}_{\text{PGW}}$-$\text{Threshold}_{\text{Past}}$ ("Threshold Change"). All mountain subdomains are analyzed on d02 (12-km grid spacing) with the exception of the Wasatch and Colorado Rockies, which are analyzed on d03 (4-km grid spacing). For each subdomain, P_{40} indicates the 40^{th} percentile of mean April SWE used to constrain analysis. P_{40} Area is the percentage of grid points analyzed in each subdomain.

Mountain Subdomain	$\text{Threshold}_{\text{Past}}$ (m)	$\text{Threshold}_{\text{PGW}}$ (m)	Threshold Change (m)	P_{40} (mm)	P_{40} Area (%)
Washington Cascades	1574 ± 81	1904 ± 141	330	430	56
Sierra Nevada	2083 ± 84	2387 ± 88	304	33	47
Northern Rockies	1595 ± 38	1858 ± 88	263	78	51
Middle Rockies	1805 ± 72	2252 ± 35	447	101	57
Wasatch	1946 ± 20	2263 ± 25	317	56	48
Colorado Rockies	2119 ± 64	2358 ± 45	239	41	56

Table 3.2. The Snow Telemetry (SNOTEL) sites used in the validation of WRF_{Past} performance in Fig. 3.3a. All sites are in the state of Utah. Data span 1995-2004 for all sites.

Station ID	Name	Elevation (m)	Latitude (°N)	Longitude (°W)
330	Beaver Divide	2524	40.6	111.1
332	Ben Lomond Peak	2438	41.4	111.9
333	Ben Lomond Trail	1777	41.4	111.9
366	Brighton	2667	40.6	111.6
371	Buck Flat	2874	39.1	111.4
374	Bug Lake	2423	41.7	111.4
393	Chalk Creek 2	2487	40.9	111.1
399	Clear Creek 1	2715	39.9	111.3
432	Currant Creek	2438	40.4	111.1
435	Daniels-Strawberry	2450	40.3	111.3
444	Dill's Camp	2799	39.0	111.5
455	Dry Bread Pond	2545	41.4	111.5
471	Emigrant Summit	2252	42.4	111.6
484	Franklin Basin	2490	42.1	111.6
493	Giveout	2112	42.4	111.2
896	Hardscrabble	2210	40.9	111.7
533	Horse Ridge	2487	41.3	111.4
582	Little Bear	1995	41.4	111.8
596	Lookout Peak	2499	40.8	111.7
612	Mammoth-Cottonwood	2660	39.7	111.3
628	Mill-D North	2733	40.7	111.6
634	Monte Cristo	2731	41.5	111.5
684	Parley's Summit	2286	40.8	111.6
742	Seeley Creek	3021	39.3	111.4
763	Smith Morehouse	2316	40.8	111.1
795	Strawberry Divide	2476	40.2	111.2
814	Thaynes Canyon	2813	40.6	111.5
820	Timpanogos Divide	2481	40.4	111.6
823	Tony Grove Lake	2583	41.9	111.6

CHAPTER 4

DISCUSSION AND CONCLUSIONS

This study featured analysis from high-resolution dynamical downscaling simulations of both past and future climate of the western United States. The historical simulation validated well with respect to observations but noteworthy relationships exist between the precipitation bias over the Wasatch Mountains and synoptic flow regimes. The two characteristic regimes leading to large wet and dry bias days are distinctly associated with reanalysis-relative biases that help explain daily and seasonal precipitation errors. The future climate simulation applied a pseudo-global warming strategy by perturbing historical reanalysis with a high-confidence version of future climate. The dynamically downscaled version of this climate change signal led to clean comparison with the historical simulation's spring snowpack variability. The geographic variations in the uniformly positive rising threshold elevation below which temperature drives snowpack variability indicate mountain range-specific impacts to hydrologic systems under a changing climate.

An additional implication of this study is that changes in the mid-latitude storm track may influence the bias in WRF-downscaled simulations of future precipitation over the Wasatch Mountains and potentially elsewhere. Changes in the frequency of

northern Pacific Northwest-landfalling midlatitude cyclones, which cause deep inland penetration of strong moisture along strong geopotential height gradients, may yield future biases that differ from those in this historical simulation. This is an important consideration in light of the evolving past and future synoptic pathways driving wintertime Wasatch precipitation, such as the poleward shift of storm tracks under a changing climate (Yin, 2005; Christensen et al., 2013). Specific to our domain, Gillies et al. (2012) describe the trends in frequency of the two archetypal storm systems which produce approximately 93% of accumulated Utah-wide precipitation from January to March. Their "subtropical jet-type" system resembles closely the synoptic pattern that produces large wet precipitation biases in our simulation, and their "trough-type" system resembles the synoptic pattern that produces large dry biases in our simulation (see their Fig. 9). While the historical trends in the storm frequency and storm total precipitation of the "subtropical jet-type" (our wet-bias) regime are not statistically significant, the "trough-type" (our dry-bias) regime has declined by 3-5 precipitation-producing events per year over the past five decades, while storm total precipitation has risen approximately 14% per event over that same period. These trends highlight the importance of considering evolving storm tracks and storm characteristics arising from both natural variability and climate change when assessing the accuracy of GCM precipitation output.

Our PGW method did not alter the timing and number of midlatitude cyclones but rather perturbed the initial and boundary conditions of WRF with a medium-high emission scenario's decadal monthly average climate change signal of

temperature, humidity, and SST change. This isolated a high-confidence feature of climate change (warming and moistening) while avoiding aspects of storm track shift that produce highly varied precipitation outcomes among ensemble members (Deser et al., 2014). Important insights may be available by extending this analysis to either statistically or dynamically downscaled ensembles of global climate model simulations over a range of emission scenarios. Additional PGW simulations are warranted for comparison to this one as well, including different emission scenarios (i.e., RCP 8.5) or other perturbed parameters (geopotential height, wind components). Simulations of future climate which apply dynamical downscaling to CCSM4 are underway and offer a compelling comparative data set with respect to the PGW simulation as well.

Other applications of these historical and future simulations include a decomposition and analysis of the water balance of the Wasatch region pursuant to a clearer understanding of the impact of climate change on future timing and magnitude of runoff. Analysis of historical trends and future change in evapotranspiration in the Salt Lake Valley and surrounding region may also provide important considerations for water management in light of a growing population and evolving water demand. Overall, this framework of high-resolution dynamical downscaling of past and future climate is proven effective and useful for hydrologic research and other applications.

REFERENCES

Abatzoglou, J. T., 2011: Influence of the PNA on declining mountain snowpack in the western United States. *Int. J. Climatol.*, **31 (8)**, 1135–1142, URL http://dx.doi.org/10.1002/joc.2137.

Alcott, T. I., W. J. Steenburgh, and N. F. Laird, 2012: Great Salt Lake effect precipitation: Observed frequency, characteristics, and associated environmental factors. *Wea. Forecasting*, **27 (4)**, 954–971, doi:10.1175/WAF-D-12-00016.1, URL http://dx.doi.org/10.1175/WAF-D-12-00016.1.

Bao, X. and F. Zhang, 2013: Evaluation of NCEP–CFSR, NCEP–NCAR, ERA-Interim, and ERA-40 reanalysis datasets against independent sounding observations over the Tibetan Plateau. *Journal of Climate*, **26 (1)**, 206–214.

Bardsley, T., A. Wood, M. Hobbins, T. Kirkham, L. Briefer, J. Niermeyer, and S. Burian, 2013: Planning for an uncertain future: Climate change sensitivity assessment toward adaptation planning for public water supply. *Earth Interact.*, **17 (23)**, 1–26, doi:10.1175/2012EI000501.1, URL http://dx.doi.org/10.1175/2012EI000501.1.

Brown, R. D. and P. W. Mote, 2009: The response of Northern Hemisphere snow cover to a changing climate. *JOURNAL OF CLIMATE*, **22 (8)**, 2124–2145, doi:10.1175/2008JCLI2665.1.

Caldwell, P., H.-N. Chin, D. Bader, and G. Bala, 2009: Evaluation of a WRF dynamical downscaling simulation over California. *Climatic Change*, **95 (3-4)**, 499–521, doi:10.1007/s10584-009-9583-5, URL http://dx.doi.org/10.1007/s10584-009-9583-5.

Cayan, D. R., 1996: Interannual climate variability and snowpack in the western United States. *J. Climate*, **9 (5)**, 928–948, doi:10.1175/1520-0442(1996)009¡0928:ICVASI¿2.0.CO;2, URL http://dx.doi.org/10.1175/1520-0442(1996)009<0928:ICVASI>2.0.CO;2.

Chen, F. and J. Dudhia, 2001: Coupling an advanced land surface hydrology model with the Penn State NCAR MM5 Modeling System. Part I: Model implementation and sensitivity. *Mon. Wea. Rev.*, **129 (4)**, 569–585, doi:10.1175/1520-0493(2001)129¡0569:CAALSH¿2.0.CO;2, URL http://dx.doi.org/10.1175/1520-0493(2001)129<0569:CAALSH>2.0.CO;2.

Christensen, J., et al., 2013: *Climate Phenomena and their Relevance for Future Regional Climate Change*, book section 14, 12171308. Cambridge University Press, Cambridge, United Kingdom and New York, NY, USA, doi: 10.1017/CBO9781107415324.028, URL www.climatechange2013.org.

Collins, W. D., et al., 2006: The Community Climate System Model Version 3 (CCSM3). *J. Climate*, **19 (11)**, 2122–2143, doi:10.1175/JCLI3761.1, URL http://dx.doi.org/10.1175/JCLI3761.1.

Daly, C., W. P. Gibson, G. H. Taylor, G. L. Johnson, and P. Pasteris, 2002: A knowledge-based approach to the statistical mapping of climate. *Climate research*, **22 (2)**, 99–113.

Daly, C., M. Halbleib, J. I. Smith, W. P. Gibson, M. K. Doggett, G. H. Taylor, J. Curtis, and P. P. Pasteris, 2008: Physiographically sensitive mapping of climatological temperature and precipitation across the conterminous United States. *International Journal of Climatology*, **28 (15)**, 2031–2064, doi:10.1002/joc.1688, URL http://dx.doi.org/10.1002/joc.1688.

Daly, C., R. P. Neilson, and D. L. Phillips, 1994: A statistical-topographic model for mapping climatological precipitation over mountainous terrain. *Journal of applied meteorology*, **33 (2)**, 140–158.

Daly, C., G. Taylor, and W. Gibson, 1997: The PRISM approach to mapping precipitation and temperature. *Proc., 10th AMS Conf. on Applied Climatology*, 20–23.

Deser, C., R. Knutti, S. Solomon, and A. S. Phillips, 2012: Communication of the role of natural variability in future North American climate. *Nature Clim. Change*, **2 (11)**, 775–779, URL http://dx.doi.org/10.1038/nclimate1562.

Deser, C., A. S. Phillips, M. A. Alexander, and B. V. Smoliak, 2014: Projecting North American climate over the next 50 years: Uncertainty due to internal variability*. *J. Climate*, **27 (6)**, 2271–2296, doi:10.1175/JCLI-D-13-00451.1, URL http://dx.doi.org/10.1175/JCLI-D-13-00451.1.

Ebisuzaki, W. and L. Zhang, 2011: Assessing the performance of the CFSR by an ensemble of analyses. *Climate Dynamics*, **37 (11)**, 2541–2550, doi:10.1007/s00382-011-1074-5, URL http://dx.doi.org/10.1007/s00382-011-1074-5.

Erler, A. R., W. R. Peltier, and M. DOrgeville, 2014: Dynamically downscaled high-resolution hydroclimate projections for western Canada. *J. Climate*, **28 (2)**, 423–450, doi:10.1175/JCLI-D-14-00174.1, URL http://dx.doi.org/10.1175/JCLI-D-14-00174.1.

Freedman, D. and P. Diaconis, 1981: On the histogram as a density estimator: L 2 theory. *Zeitschrift fr Wahrscheinlichkeitstheorie und Verwandte Gebiete*, **57 (4)**, 453–476, doi:10.1007/BF01025868, URL http://dx.doi.org/10.1007/BF01025868.

Gent, P. R., et al., 2011: The Community Climate System Model version 4. *J. Climate*, **24 (19)**, 4973–4991, doi:10.1175/2011JCLI4083.1, URL http://dx.doi.org/10.1175/2011JCLI4083.1.

Gillies, R. R., S.-Y. Wang, and M. R. Booth, 2012: Observational and synoptic analyses of the winter precipitation regime change over Utah. *J. Climate*, **25 (13)**, 4679–4698, doi:10.1175/JCLI-D-11-00084.1, URL http://dx.doi.org/10.1175/JCLI-D-11-00084.1.

Groisman, P. Y. and D. R. Easterling, 1994: Variability and trends of total precipitation and snowfall over the United States and Canada. *J. Climate*, **7 (1)**, 184–205, doi:10.1175/1520-0442(1994)007¡0184:VATOTP¿2.0.CO;2, URL http://dx.doi.org/10.1175/1520-0442(1994)007<0184:VATOTP>2.0.CO;2.

Gutmann, E. D., R. M. Rasmussen, C. Liu, K. Ikeda, D. J. Gochis, M. P. Clark, J. Dudhia, and G. Thompson, 2012: A comparison of statistical and dynamical downscaling of winter precipitation over complex terrain. *Journal of Climate*, **25 (1)**, 262 – 281.

Hamlet, A. F., P. W. Mote, M. P. Clark, and D. P. Lettenmaier, 2005: Effects of temperature and precipitation variability on snowpack trends in the western United States. *J. Climate*, **18 (21)**, 4545–4561, doi:10.1175/JCLI3538.1, URL http://dx.doi.org/10.1175/JCLI3538.1.

Harding, B. L., A. W. Wood, and J. R. Prairie, 2012: The implications of climate change scenario selection for future streamflow projection in the Upper Colorado River Basin. *Hydrology and Earth System Sciences*, **16 (11)**, 3989–4007, doi:10.5194/hess-16-3989-2012, URL http://www.hydrol-earth-syst-sci.net/16/3989/2012/.

Harnik, N., R. Seager, N. Naik, M. Cane, and M. Ting, 2010: The role of linear wave refraction in the transient eddy mean flow response to tropical Pacific SST anomalies. *Quarterly Journal of the Royal Meteorological Society*, **136 (653)**, 2132–2146, doi:10.1002/qj.688, URL http://dx.doi.org/10.1002/qj.688.

Hidalgo, H. G., M. D. Dettinger, and D. R. Cayan, 2008: Downscaling with constructed analogues: Daily precipitation and temperature fields over the United States. *California Energy Commission PIER Final Project Report CEC-500-2007-123*.

Hoerling, M. P. and A. Kumar, 2002: Atmospheric response patterns associated with tropical forcing. *J. Climate*, **15 (16)**, 2184–

2203, doi:10.1175/1520-0442(2002)015¡2184:ARPAWT¿2.0.CO;2, URL http://dx.doi.org/10.1175/1520-0442(2002)015<2184:ARPAWT>2.0.CO;2.

Hofer, M., B. Marzeion, and T. Mlg, 2012: Comparing the skill of different reanalyses and their ensembles as predictors for daily air temperature on a glaciated mountain (Peru). *Climate Dynamics*, **39 (7-8)**, 1969–1980, URL http://www.ncbi.nlm.nih.gov/pmc/articles/PMC4461156/.

Ikeda, K., et al., 2010: Simulation of seasonal snowfall over Colorado. *Atmospheric Research*, **97 (4)**, 462 – 477, doi:http://dx.doi.org/10.1016/j.atmosres.2010.04.010, URL http://www.sciencedirect.com/science/article/pii/S0169809510001043, from the Lab to Models and Global Observations: Hans R. Pruppacher and Cloud PhysicsHans R. Pruppacher and Cloud Physics.

Janjic, Z. I., 1994: The step-mountain eta coordinate model: Further developments of the convection, viscous sublayer, and turbulence closure schemes. *Monthly Weather Review*, **122 (5)**, 927–945.

Janjić, Z. I., 2002: Nonsingular implementation of the Mellor-Yamada level 2.5 scheme in the NCEP Meso model. *NCEP office note*, **437**, 61.

Julander, R. P. and M. Bricco, 2006: An examination of external influences embedded in the historical snow course data of Utah. *All U.S. Government Documents (Utah Regional Depository)*.

Kapnick, S. and A. Hall, 2012: Causes of recent changes in western North American snowpack. *Climate Dynamics*, **38 (9-10)**, 1885–1899, doi:10.1007/s00382-011-1089-y, URL http://dx.doi.org/10.1007/s00382-011-1089-y.

Kawase, H., T. Yoshikane, M. Hara, F. Kimura, T. Yasunari, B. Ailikun, H. Ueda, and T. Inoue, 2009: Intermodel variability of future changes in the Baiu rainband estimated by the pseudo global warming downscaling method. *Journal of Geophysical Research: Atmospheres*, **114 (D24)**, n/a–n/a, doi:10.1029/2009JD011803, URL http://dx.doi.org/10.1029/2009JD011803, d24110.

Kim, H.-M., P. J. Webster, and J. A. Curry, 2012: Seasonal prediction skill of ECMWF System 4 and NCEP CFSv2 retrospective forecast for the Northern Hemisphere winter. *Climate Dynamics*, **39 (12)**, 2957–2973.

Klos, P. Z., T. E. Link, and J. T. Abatzoglou, 2014: Extent of the rain-snow transition zone in the western U.S. under historic and projected climate. *Geophysical Research Letters*, **41 (13)**, 4560–4568, doi:10.1002/2014GL060500, URL http://dx.doi.org/10.1002/2014GL060500.

Knowles, N., M. D. Dettinger, and D. R. Cayan, 2006: Trends in snowfall versus rainfall in the western United States. *J. Climate*, **19 (18)**, 4545–4559, doi:10.1175/JCLI3850.1, URL http://dx.doi.org/10.1175/JCLI3850.1.

Kumar, S., V. Merwade, J. L. Kinter, and D. Niyogi, 2013: Evaluation of temperature and precipitation trends and long-term persistence in CMIP5 twentieth-century climate simulations. *J. Climate*, **26 (12)**, 4168–4185, doi:10.1175/JCLI-D-12-00259.1, URL http://dx.doi.org/10.1175/JCLI-D-12-00259.1.

Lee, D. E. and M. Biasutti, 2014: Climatology and variability of precipitation in the twentieth-century reanalysis. *J. Climate*, **27 (15)**, 5964–5981, doi:10.1175/JCLI-D-13-00630.1, URL http://dx.doi.org/10.1175/JCLI-D-13-00630.1.

Liu, C., K. Ikeda, G. Thompson, R. Rasmussen, and J. Dudhia, 2011: High-resolution simulations of wintertime precipitation in the Colorado Headwaters region: Sensitivity to physics parameterizations. *Mon. Wea. Rev.*, **139 (11)**, 3533–3553, doi:10.1175/MWR-D-11-00009.1, URL http://dx.doi.org/10.1175/MWR-D-11-00009.1.

Maurer, E. P., H. G. Hidalgo, T. Das, M. D. Dettinger, and D. R. Cayan, 2010: The utility of daily large-scale climate data in the assessment of climate change impacts on daily streamflow in California. *Hydrology and Earth System Sciences*, **14 (6)**, 1125–1138, doi:10.5194/hess-14-1125-2010, URL http://www.hydrol-earth-syst-sci.net/14/1125/2010/.

McCabe, G. and D. Wolock, 2010: Long-term variability in Northern Hemisphere snow cover and associations with warmer winters. *Climatic Change*, **99 (1-2)**, 141–153, doi:10.1007/s10584-009-9675-2, URL http://dx.doi.org/10.1007/s10584-009-9675-2.

McCabe, G. J. and D. M. Wolock, 1999: General-circulation-model simulations of future snowpack in the western United States. *JAWRA Journal of the American Water Resources Association*, **35 (6)**, 1473–1484, doi:10.1111/j.1752-1688.1999.tb04231.x, URL http://dx.doi.org/10.1111/j.1752-1688.1999.tb04231.x.

McMillen, J. D. and W. J. Steenburgh, 2014: Impact of microphysics parameterizations on simulations of the 27 October 2010 Great Salt Lake effect snowstorm. *Wea. Forecasting*, **30 (1)**, 136–152, doi:10.1175/WAF-D-14-00060.1, URL http://dx.doi.org/10.1175/WAF-D-14-00060.1.

Morán-Tejeda, E., J. I. Lpez-Moreno, and M. Beniston, 2013: The changing roles of temperature and precipitation on snowpack variability in Switzerland as a function of altitude. *Geophys. Res. Lett.*, **40 (10)**, 2131–2136, URL http://dx.doi.org/10.1002/grl.50463.

Mote, P. W., 2006: Climate-driven variability and trends in mountain snowpack in western North America. *J. Climate*, **19 (23)**, 6209–6220, doi:10.1175/JCLI3971.1, URL http://dx.doi.org/10.1175/JCLI3971.1.

Mote, P. W., A. F. Hamlet, M. P. Clark, and D. P. Lettenmaier, 2005: Declining mountain snowpack in western North America. *Bull. Amer. Meteor. Soc.*, **86 (1)**, 39–49, doi:10.1175/BAMS-86-1-39, URL http://dx.doi.org/10.1175/BAMS-86-1-39.

Orlanski, I., 2005: A new look at the Pacific storm track variability: Sensitivity to tropical SSTs and to upstream seeding. *J. Atmos. Sci.*, **62 (5)**, 1367–1390, doi:10.1175/JAS3428.1, URL http://dx.doi.org/10.1175/JAS3428.1.

Peacock, S., 2012: Projected twenty-first-century changes in temperature, precipitation, and snow cover over North America in CCSM4. *J. Climate*, **25 (13)**, 4405–4429, doi:10.1175/JCLI-D-11-00214.1, URL http://dx.doi.org/10.1175/JCLI-D-11-00214.1.

Pederson, G. T., J. L. Betancourt, and G. J. McCabe, 2013: Regional patterns and proximal causes of the recent snowpack decline in the Rocky Mountains, U.S. *Geophysical Research Letters*, **40 (9)**, 1811–1816, doi:10.1002/grl.50424, URL http://dx.doi.org/10.1002/grl.50424.

Pederson, G. T., et al., 2011: The unusual nature of recent snowpack declines in the North American Cordillera. *Science*, **333 (6040)**, 332–335, doi:10.1126/science.1201570, URL http://www.sciencemag.org/content/333/6040/332.abstract, http://www.sciencemag.org/content/333/6040/332.full.pdf.

Pierce, D. W. and D. R. Cayan, 2012: The uneven response of different snow measures to human-induced climate warming. *J. Climate*, **26 (12)**, 4148–4167, doi:10.1175/JCLI-D-12-00534.1, URL http://dx.doi.org/10.1175/JCLI-D-12-00534.1.

Pierce, D. W., et al., 2008: Attribution of declining western U.S. snowpack to human effects. *J. Climate*, **21 (23)**, 6425–6444, doi:10.1175/2008JCLI2405.1, URL http://dx.doi.org/10.1175/2008JCLI2405.1.

Ramamurthy, P. and E. R. Pardyjak, 2011: Toward understanding the behavior of carbon dioxide and surface energy fluxes in the urbanized semi-arid Salt Lake Valley, Utah, USA. *Atmospheric Environment*, **45 (1)**, 73 – 84, doi:http://dx.doi.org/10.1016/j.atmosenv.2010.09.049, URL http://www.sciencedirect.com/science/article/pii/S1352231010008356.

Rasmussen, R., et al., 2011a: High-resolution coupled climate runoff simulations of seasonal snowfall over Colorado: A process study of current and warmer climate. *J. Climate*, **24 (12)**, 3015–3048, doi:10.1175/2010JCLI3985.1, URL http://dx.doi.org/10.1175/2010JCLI3985.1.

Rasmussen, R., et al., 2011b: How well are we measuring snow: The NOAA/FAA/NCAR winter precipitation test bed. *Bull. Amer. Meteor. Soc.*, **93 (6)**, 811–829, doi:10.1175/BAMS-D-11-00052.1, URL http://dx.doi.org/10.1175/BAMS-D-11-00052.1.

Rasmussen, R., et al., 2014: Climate change impacts on the water balance of the Colorado Headwaters: High-resolution regional climate model simulations. *J. Hydrometeor*, **15 (3)**, 1091–1116, doi:10.1175/JHM-D-13-0118.1, URL http://dx.doi.org/10.1175/JHM-D-13-0118.1.

Rayner, N. A., D. E. Parker, E. B. Horton, C. K. Folland, L. V. Alexander, D. P. Rowell, E. C. Kent, and A. Kaplan, 2003: Global analyses of sea surface temperature, sea ice, and night marine air temperature since the late nineteenth century. *Journal of Geophysical Research: Atmospheres*, **108 (D14)**, n/a–n/a, doi:10.1029/2002JD002670, URL http://dx.doi.org/10.1029/2002JD002670, 4407.

Rutz, J. J., W. J. Steenburgh, and F. M. Ralph, 2013: Climatological characteristics of atmospheric rivers and their inland penetration over the western United States. *Mon. Wea. Rev.*, **142 (2)**, 905–921, doi:10.1175/MWR-D-13-00168.1, URL http://dx.doi.org/10.1175/MWR-D-13-00168.1.

Saha, S., et al., 2010: The NCEP Climate Forecast System Reanalysis. *Bull. Amer. Meteor. Soc.*, **91 (8)**, 1015–1057, doi:10.1175/2010BAMS3001.1, URL http://dx.doi.org/10.1175/2010BAMS3001.1.

Schär, C., C. Frei, D. Lthi, and H. C. Davies, 1996: Surrogate climate-change scenarios for regional climate models. *Geophys. Res. Lett.*, **23 (6)**, 669–672, URL http://dx.doi.org/10.1029/96GL00265.

Seager, R., N. Harnik, Y. Kushnir, W. Robinson, and J. Miller, 2003: Mechanisms of hemispherically symmetric climate variability. *J. Climate*, **16 (18)**, 2960–2978, doi:10.1175/1520-0442(2003)016¡2960:MOHSCV¿2.0.CO;2, URL http://dx.doi.org/10.1175/1520-0442(2003)016<2960:MOHSCV>2.0.CO;2.

Seager, R., N. Naik, M. Ting, M. A. Cane, N. Harnik, and Y. Kushnir, 2010: Adjustment of the atmospheric circulation to tropical Pacific SST anomalies: Variability of transient eddy propagation in the Pacific North America sector. *Quarterly Journal of the Royal Meteorological Society*, **136 (647)**, 277–296, doi:10.1002/qj.588, URL http://dx.doi.org/10.1002/qj.588.

Serreze, M. C., M. P. Clark, R. L. Armstrong, D. A. McGinnis, and R. S. Pulwarty, 1999: Characteristics of the western United States snowpack from snowpack telemetry (SNOTEL) data. *Water Resources Research*, **35 (7)**, 2145–2160, doi:10.1029/1999WR900090, URL http://dx.doi.org/10.1029/1999WR900090.

Sharp, E., P. Dodds, M. Barrett, and C. Spataru, 2015: Evaluating the accuracy of CFSR reanalysis hourly wind speed forecasts for the UK

using in situ measurements and geographical information. *Renewable Energy*, **77**, 527 – 538, doi:http://dx.doi.org/10.1016/j.renene.2014.12.025, URL http://www.sciencedirect.com/science/article/pii/S0960148114008520.

Skamarock, W. C., et al., 2008: A description of the Advanced Research WRF Version 3. Tech. rep., National Center for Atmospheric Research, 1–113 pp.

Smith, K., C. Strong, and S.-Y. Wang, 2015: Connectivity between historical Great Basin precipitation and Pacific Ocean variability: A CMIP5 model evaluation. *J. Climate*, **28 (15)**, 6096–6112, doi:10.1175/JCLI-D-14-00488.1, URL http://dx.doi.org/10.1175/JCLI-D-14-00488.1.

Sospedra-Alfonso, R., J. R. Melton, and W. J. Merryfield, 2015: Effects of temperature and precipitation on snowpack variability in the central Rocky Mountains as a function of elevation. *Geophysical Research Letters*, **42 (11)**, 4429–4438, doi:10.1002/2015GL063898, URL http://dx.doi.org/10.1002/2015GL063898, 2015GL063898.

Steenburgh, W. J., S. F. Halvorson, and D. J. Onton, 2000: Climatology of lake-effect snowstorms of the Great Salt Lake. *Mon. Wea. Rev.*, **128 (3)**, 709–727, doi:10.1175/1520-0493(2000)128¡0709:COLESO¿2.0.CO;2, URL http://dx.doi.org/10.1175/1520-0493(2000)128<0709:COLESO>2.0.CO;2.

Steenburgh, W. J. and D. J. Onton, 2001: Multiscale analysis of the 7 December 1998 Great Salt Lake effect snowstorm. *Mon. Wea. Rev.*, **129 (6)**, 1296–1317, doi:10.1175/1520-0493(2001)129¡1296:MAOTDG¿2.0.CO;2, URL http://dx.doi.org/10.1175/1520-0493(2001)129<1296:MAOTDG>2.0.CO;2.

Stocker, T., et al., 2013: *Technical Summary*, book section TS, 33115. Cambridge University Press, Cambridge, United Kingdom and New York, NY, USA, doi:10.1017/CBO9781107415324.005, URL www.climatechange2013.org.

Strong, C., A. K. Kochanski, and E. T. Crosman, 2014: A slab model of the Great Salt Lake for regional climate simulation. *J. Adv. Model. Earth Syst.*, **6 (3)**, 602–615, URL http://dx.doi.org/10.1002/2014MS000305.

Thompson, G., P. R. Field, R. M. Rasmussen, and W. D. Hall, 2008: Explicit forecasts of winter precipitation using an improved bulk microphysics scheme. part ii: Implementation of a new snow parameterization. *Mon. Wea. Rev.*, **136 (12)**, 5095–5115, doi:10.1175/2008MWR2387.1, URL http://dx.doi.org/10.1175/2008MWR2387.1.

Wolock, D. M. and G. J. McCabe, 1999: Estimates of runoff using water-balance and atmospheric general circulation models1. *JAWRA Journal of the American Water Resources Association*, **35 (6)**, 1341–1350, doi:10.1111/j.1752-1688.1999.tb04219.x, URL http://dx.doi.org/10.1111/j.1752-1688.1999.tb04219.x.

Yang, D., B. E. Goodison, J. R. Metcalfe, V. S. Golubev, R. Bates, T. Pangburn, and C. L. Hanson, 1998: Accuracy of NWS 8" standard nonrecording precipitation gauge: Results and application of WMO intercomparison. *J. Atmos. Oceanic Technol.*, **15 (1)**, 54–68, doi:10.1175/1520-0426(1998)015¡0054:AONSNP¿2.0.CO;2, URL http://dx.doi.org/10.1175/1520-0426(1998)015<0054:AONSNP>2.0.CO;2.

Yeager, K. N., W. J. Steenburgh, and T. I. Alcott, 2012: Contributions of lake-effect periods to the cool-season hydroclimate of the Great Salt Lake Basin. *J. Appl. Meteor. Climatol.*, **52 (2)**, 341–362, doi:10.1175/JAMC-D-12-077.1, URL http://dx.doi.org/10.1175/JAMC-D-12-077.1.

Yin, J. H., 2005: A consistent poleward shift of the storm tracks in simulations of 21st century climate. *Geophysical Research Letters*, **32 (18)**.

Yoon, J.-H., L. Ruby Leung, and J. Correia, 2012: Comparison of dynamically and statistically downscaled seasonal climate forecasts for the cold season over the United States. *Journal of Geophysical Research: Atmospheres*, **117 (D21)**, n/a–n/a, doi:10.1029/2012JD017650, URL http://dx.doi.org/10.1029/2012JD017650, d21109.